

Sublimation of ice-tholins mixtures: a morphological and spectrophotometric study

Olivier Poch^{1*}, Antoine Pommerol², Bernhard Jost², Nathalie Carrasco^{3,4}, Cyril Szopa³ and
Nicolas Thomas²

¹ Center for Space and Habitability, Universität Bern, Sidlerstrasse, 5, 3012 Bern, Switzerland

² Physikalisches Institut, Universität Bern, Sidlerstrasse, 5, 3012 Bern, Switzerland

³ Université Versailles St-Quentin ; Sorbonne Universités, UPMC Univ. Paris 06 ;
CNRS/INSU, LATMOS-IPSL, 11 Boulevard d'Alembert, 78280 Guyancourt, France

⁴ Institut Universitaire de France, 103 Bvd St-Michel, 75005 Paris, France

*To whom correspondence should be addressed:

Physikalisches Institut, Universität Bern

Sidlerstrasse, 5

CH-3012 Bern, Switzerland

olivier.poch@csh.unibe.ch

+44 31 631 33 93

Manuscript accepted for publication in *Icarus*

Abstract:

Sublimation, the direct transition from solid to gas phase, is a process responsible for shaping and changing the reflectance properties of many Solar System surfaces. In this study, we have characterized the evolution of the structure/texture and of the visible and near-infrared (VIS-NIR) spectral reflectance of surfaces made of water ice mixed with analogues of complex extraterrestrial organic matter, named *tholins*, under low temperature ($<-70^{\circ}\text{C}$) and pressure (10^{-5} mbar) conditions. The experiments were carried out in the SCITEAS simulation setup recently built as part of the Laboratory for Outflow Studies of Sublimating Materials (LOSSy) at the University of Bern (Pommerol *et al.*, 2015a). As the water ice sublimated, we observed *in situ* the formation of a sublimation lag deposit made of a water-free porous ($>90\%$ porosity) network of organic filaments on top of the ice. The temporal evolution of the tholins and water ice spectral features (reflectance at the absorption bands wavelengths, red slope, from 0.40 to 1.90 μm) are analysed throughout the sublimation of the samples. We studied how different mixtures of tholins with water (0.1 wt.% tholins as coating or inclusions within the water particles), and different ice particle sizes (4.5 ± 2.5 or 67 ± 31 μm) influence the morphological and spectral evolutions of the samples. The sublimation of the ice below the mantle produces a gas flow responsible for the ejection of mm to cm-sized fragments of the deposit in outbursts-like events. The results show remarkable differences between these samples in term of mantle structure, speed of mantle building, rates and surface area of mantle ejections. These data provide useful references for interpreting remote-sensing observations of icy Solar System surfaces, in particular the activity of comet nuclei where sublimation of organic-rich ices and deposition of organic-dust particles likely play a major role. Consequently, the data presented here could be of high interest for the interpretation of Rosetta, and also New Horizons, observations.

Keywords: Ices; Comets, dust; Comets, nucleus; Trans-neptunian objects; Spectroscopy

1. Introduction

The surfaces of many objects in the Solar System comprise substantial quantities of water ice either in pure form or mixed with mineral and/or organic molecules. Missions exploring these objects usually carry imaging systems and spectrometers which require a good knowledge of the spectro-photometric properties of ice to allow appropriate interpretation. Both numerical models and laboratory experiments are used to overcome this challenge. This paper presents laboratory experiments focusing on the evolution of the optical properties of surfaces composed of water ice and complex organic matter during the sublimation of the water ice.

Water ice is found associated with organics in many objects of the Solar System. Comets are probably the most striking examples, because they possess a high mass ratio of organics compared to ice, estimated from 0.1 to 1. (Fomenkova, 1999; Huebner, 2003; Jessberger *et al.*, 1989; Kuppers *et al.*, 2005; Marboeuf *et al.*, 2014; Weiler *et al.*, 2004). Recent observations of comet 67P/Churyumov-Gerasimenko by the Rosetta spacecraft suggest a surface dominated by organic materials with water ice near the surface (Altwegg *et al.*, 2015; Thomas *et al.*, 2015). The icy satellites of Jupiter (Europa, Ganymede, Callisto) and Saturn (Titan, Iapetus) (Moore *et al.*, 2009), as well as the Trans-neptunian Objects (TNOs) (including Kuiper belt objects, KBOs) and Centaurs (Duffard *et al.*, 2014) also probably have a surface consisting of ice mixed with organics, but at a lower mass ratio than comets. The surface of the Saturn's moon Titan contains a large amount of organics and possibly some water ice, but there is no definitive spectral evidence for water ice exposed at the surface (see Neish *et al.*, 2015 and references herein). Finally, even very close to the Sun, the ice deposits on Mercury have been hypothesized to be locally covered by organic matter partly because of their probable cometary origin (Paige *et al.*, 2013). The complex organic matter present in those different environments has been synthesized (endogenously or exogenously) from smaller molecules in the gas or solid phase.

In the gas phase, solid macromolecular carbonaceous products are efficiently formed after the irradiation of a reduced or neutral gas mixture composed of CH₄, N₂, CO, etc. The breakdown of these simple molecules by energetic particles (VUV/UV photons, electrons, ions) followed by the recombination of their fragments lead to the production of increasingly heavy organic molecules, and finally to solid aerosols. This process has only been observed in the laboratory experiments and in Titan's atmosphere, but it probably occurs on other

planetary bodies having thin atmospheres, such as Triton and Pluto (Cruikshank, 2005; Cruikshank *et al.*, 2015; McDonald *et al.*, 1994). The analogue solid organic residues produced after irradiation of a gas mixture composed of simple molecules in the laboratory have been named “*tholins*” by Sagan and Khare (1979). It is derived from the Greek θόλος meaning “muddy”, in reference to the orange-brownish colour of the material.

In the solid phase, such solid organic residues can also be produced via energetic processing of ice mixtures (such as VUV/UV photons, cosmic rays and thermal processes), although less efficiently than in the gas phase. Similarly as in the gas phase, the irradiation of simple molecules (H₂O, CO, CH₄, NH₃, CH₃OH, etc.) in the form of ices can produce radicals that recombine within the ice to form higher mass molecules, up to macromolecular substances which are called organic refractory matter. Many laboratory experiments performed since 1961 have proved that virtually any carbon-containing ice produces organics upon irradiation (Berger, 1961; Thompson *et al.*, 1987 and references herein). As the irradiation doses or energies are increased, more refractory and darker carbonaceous compounds can be formed (Andronico *et al.*, 1987; Thompson *et al.*, 1987). The thermal processing of the ices also contributes to the production of complex refractory organics. Icy dust particles that formed the pre-solar nebula underwent such irradiation and thermal processing before being incorporated to comets and planetesimals (Herbst and Van Dishoeck, 2009). Solid phase synthesis of complex organic matter may also occur currently on the surfaces of TNOs, comets and icy satellites.

The colour of these organic residues (from pale yellow, orange, brown to dark) originate from electronic transitions in the molecular orbitals of the molecules present in the residues. Electrons engaged in bonding σ , π or non-bonding n molecular orbitals can be promoted to anti-bonding orbitals σ^* or π^* by the absorption of photons in the UV-visible range. These transitions occur in specific chemical groups called chromophores. Transitions such as $\pi \rightarrow \pi^*$ and $n \rightarrow \pi^*$ occurring in π -bonds are very efficient in absorbing visible light if the molecule possesses an extended chain of π -bonds ($-\text{C}=\text{C}-$, $-\text{C}=\text{N}-$ etc.), called a conjugated system (such molecule is called an “aromatic” molecule). Other transitions such as $n \rightarrow \sigma^*$, most often centred in the ultraviolet, can also efficiently cause absorption in the visible range (Mahjoub *et al.*, 2012; Quirico *et al.*, 2008). These organic residues are made of a mixture of diverse molecules having different structures and chromophores able to absorb light in the UV-visible range. The reflectance spectra of such complex mixtures are characterized by a spectral red slope that can extend from 0.2 to 1.0 μm , with low reflectance

values in the ultraviolet and higher values as we go to the near infrared. Heavily irradiated mixtures of organics tend to preferentially lose their H, O and N heteroatoms, extend their conjugated systems and consequently become darker, a process called carbonization (Andronico *et al.*, 1987; Thompson *et al.*, 1987). The dense and highly branched carbon network resulting from this carbonization is very dark from the UV to the infrared and its spectral red slope is significantly reduced (Moroz *et al.*, 2004).

Many surfaces of primitive objects such as asteroids, comets or TNOs appear dark, with a red or neutral spectral slope, possibly because of the presence of complex organic matter at diverse stages of irradiation (Cruikshank, 2005; Cruikshank *et al.*, 2015; Cruikshank *et al.*, 2005). However, the "reddish" colour of some Solar System objects could also be explained by the presence of minerals such as iron-oxides (Singer *et al.*, 1979), sulphur polymorphs (Geissler *et al.*, 1999) or nanophase reduced iron (Clark *et al.*, 2012; Bennett *et al.*, 2013), which also exhibit such red slopes in the visible part of the spectrum. But overall, the association of ices and complex organics appears widespread and is an important aspect of many surfaces in the Solar System.

On all these objects, except Titan¹, sublimation, the direct transition from solid to gas phase, can occur, changing their surfaces and reflectance properties. It is thus essential to characterize the spectro-photometric properties of such surfaces of ices and organics when they undergo sublimation. Sublimation and the subsequent lag deposit are particularly important in the case of comets, because these ice-rich bodies approach the Sun periodically and a huge amount of ice sublimates at each of their perihelion passages. Since the closest approach of comet 1P/Halley in 1986, it is assumed that the surface of comet nuclei are mostly covered with an ice-free extremely dark mantle made of complex organic material (Hartmann *et al.*, 1987; Johnson *et al.*, 1988). Only areas representing a small fraction of the cometary surface are actively outgassing (Sekanina, 1991). The dark organic mantle covering most of the surface could be a result of sublimation process (sublimation lag deposit, or dust layer formed by re-deposition of dust lifted by cometary activity), and/or a product of the irradiation of ices by cosmic rays and solar energetic particles. Therefore, studying the building and evolution of organic sublimation lag deposits may help to understand the properties of cometary surfaces.

¹ Sublimation process is expected to be insignificant on Titan because of the high surface pressure of 1.4 atm (Fulchignoni *et al.*, 2005) and the extremely low surface temperatures.

The formation and consequences of these sublimation mantles have been the subjects of many studies, particularly in the 80's and 90's with the Comet Simulation (KOSI) project carried out at the German Aeronautic and Space Organization (DLR) (see Sears *et al.* (1999) for a review). A comet analogue of 300 mm diameter and 150 mm thick was produced by spraying suspensions of minerals in water into liquid nitrogen. Black carbon and frozen carbon dioxide were also added to this mixture. The sample was left to evolve at around 10^{-6} mbar and 210 K in a large vacuum simulation chamber, and was illuminated by Xenon-arc lamps to simulate the Sun (Grün *et al.*, 1991; Sears *et al.*, 1999). As the ices sublimed, ejection of mineral grains and ice particles was observed, followed by the build-up of an ice-free mantle made of the dust accumulating at the surface of the sample. During or after the simulations, numerous analyses were performed on the thermal conductivity of the sample, the gas emission, the observation of particles ejections and their imaging by microscopy etc. Reflectance spectra of the samples surface were also acquired before and after the simulations (from 0.5 to 2.5 μm), revealing the darkening of the sample and the decrease of the water and carbon dioxide absorptions (Oehler and Neukum, 1991). However, no measurement was performed *in situ*, during the simulation, and the ex situ analyses suffered from water frost contamination.

At the University of Bern, we have built the Laboratory for Outflow Studies of Sublimating Materials (LOSSy) with the aim of providing new insights into the spectrophotometric properties of icy planetary analogs (Pommerol *et al.*, 2015a; Pommerol *et al.*, 2011). This laboratory comprises facilities to produce icy surface analogues (water ice particles, pure or mixed with minerals and/or organics) and two setups aimed at characterizing the scattering of these surfaces: (1) the PHIRE-2 (PHysikalisches Institut Radiometry Experiment) radiogoniometer, (Pommerol *et al.*, 2011), and (2) the SCITEAS (Simulation Chamber for Imaging the Temporal Evolution of Analog Samples) simulation chamber (Pommerol *et al.*, 2015a). The SCITEAS thermal vacuum chamber enables *in situ* monitoring and spectro-photometric analyses of ice samples during sublimation at low pressure and temperature conditions found at the surface of icy Solar System objects (i.e. $T < -70^\circ\text{C}$ and $P < 10^{-5}$ mbar). In Pommerol *et al.* (2015a) we have described, in detail, the building and operations of the SCITEAS setup and analysed the data of the very first experiments performed with it. The comet #1 experiment described in Pommerol *et al.* (2015a) consisted of mixing water ice particles ($4.5 \pm 2.5 \mu\text{m}$), amorphous carbon and silicate (fine basalt powder) in liquid nitrogen, depositing this sample into SCITEAS and observing its evolution

under vacuum and low temperature. During the sublimation of the ice, movement of carbon particles was observed at the surface of the samples. Some of the movements were correlated with pressure spikes. A dark desiccated mantle developed over the ice, but the spectral signatures of the water ice persisted, partly because of the exposure of fresh water particles on the rims of circular features developing at the surface of the sample.

In the present paper, we aim to characterize how the structure/texture and the visible and near-infrared (VIS-NIR) spectral reflectance of a surface made of a mixture of water ice and complex organic matter, as a potential analogue of a cometary icy surface, evolves during the sublimation of the water ice under low temperature and pressure conditions. To do so, we have performed a series of experiments with the SCITEAS chamber. We have produced spherical ice particles of water and tholins, as analogues of complex organic matter produced in extraterrestrial environments. We have studied how the initial mixture between water and tholins and the size of the ice particles influence the properties of the deposit obtained after sublimation in term of morphology, texture and spectro-photometric properties. Our goal is to produce reference laboratory data that will be useful to interpret remote sensing datasets on icy surfaces.

2. Material and methods

2.1 SCITEAS experiment

The simulations were performed with the SCITEAS experimental setup. This simulation chamber, its imaging system and the procedure for data retrieving are briefly described in the paragraphs below. A more detailed description can be found in Pommerol *et al.* (2015a).

The SCITEAS thermal-vacuum chamber is designed to accommodate at its centre a cylindrical sample holder (160 mm diameter) containing the icy sample whose reflectance from 0.4 to 2.5 μm is continuously characterized by a hyperspectral imaging system through a 15 mm-thick fused quartz window (see Figure 1 in Pommerol *et al.*, 2015a). In order to study the sublimation of a sample over a few tens of hours, the ice samples were prepared in a

rectangular 120×60 mm sample holder with a thickness of 20 mm. The rectangular shape is inlaid in the centre of a 160 mm-diameter disk made of black anodized aluminium, inserted on top of the cylindrical holder in the simulation chamber.

Inside the chamber, the sample is maintained at cold temperature by a continuous circulation of liquid nitrogen in a cylindrical shroud, covered with a high-emissivity paint, which surrounds the sample holder at a distance of 20 mm. The chamber is evacuated using two membrane primary pumps and one turbomolecular pump. The temperatures inside the chamber are monitored via several Pt100 temperature sensors located on the shroud, on the sample holder, inside the ice samples and at the top of the ice surface. The pressure inside the chamber is monitored via a cold cathode Pirani hybrid sensor.

In the present study, the samples have been positioned 70 mm below the upper window. As a consequence, when the chamber is closed, under vacuum and cold temperature, the surface of the sample is constantly heated by infrared radiation produced by the window. Consequently, in the configuration used for the present study, thermal infrared constitutes the main energy input on the samples.

The SCITEAS Imaging System consists of a monochromatic light source (halogen lamp coupled to a monochromator), which illuminates the entire surface of the sample, and two cameras: one covering the visible spectral range (0.38–1.08 μm) and the other the near-infrared spectral range (0.85–2.5 μm). The cameras are placed 200 and 300 mm above the window of the chamber respectively, and look at the sample at an angle of about 13° from the nadir direction. The light scattered by the surface of the sample and transmitted through the window is collected by the cameras. Hyperspectral cubes of the sample surface are measured by shifting the wavelength of the incident light transmitted by the monochromator and synchronizing the acquisition of images at each wavelength by the visible and/or near-infrared camera. The hyperspectral cubes were acquired with a spectral sampling of 20 nm from 0.38 to 0.96 μm and 10 nm from 0.96 to 1.90 μm in order to better resolve the shape of the absorption bands in the near infrared. The acquisition of a complete hyperspectral cube lasts about 20 minutes.

Both external and internal calibrations were performed on the images in order to mitigate the heterogeneity of the incident light flux and the temporal variability of the sensitivity of the cameras respectively. The measured hyperspectral cubes were divided by a hyperspectral cube of a large plate of white Spectralon™ (Labsphere) placed at the position of

the sample, thereby providing a flat field correction (see Pommerol et al., 2015a). The hyperspectral cubes were then normalized by the value measured over an internal reference (small disk of Spectralon) inside each frame, for each wavelength. This normalization was done to mitigate the temporal variability of the sensitivity of the cameras which can be significant if the laboratory conditions are changing. In the reduced dataset, absolute uncertainty on the calibrated reflectance factor is ± 0.1 and the spatial variability of the reflectance across the field of view is of the order of 10%.

During the course of the experiments presented in this paper, the infrared camera suffered from stability problems. As a consequence, the infrared data presented here (in Figure 7c and Figure 8c) are degraded compared to the one presented in Pommerol *et al.* (2015a) but this does not affect the final results and conclusions. To mitigate this effect, only the most reliable infrared data have been plotted in Figure 7 and the range of wavelengths from 1.90 to 2.50 μm has been excluded in Figure 6.

2.2 Sample preparation

We have prepared several samples of water ice particles mixed with tholins in two different ways: (a) an intra-mixture, (b) an inter-mixture, in order to obtain reference laboratory data that could apply to diverse surface types and history (see section 2.2.2). Spherical water ice particles have been produced by spraying fine droplets of water into liquid nitrogen (see Figure 1). The tholins have been synthesized from CH_4 and N_2 in the gas phase (see section 2.2.1). The sample preparation is detailed in the paragraphs below and the main characteristics of the samples are summarized in Table 1.

2.2.1 Production of the tholins used for this study

In order to study the sublimation of cm-sized samples of water ice mixed with tholins, a relatively large amount of organic material (of the order of several mg) was required. The existing setups producing tholins from the irradiation of ices produce thin films consisting of only some micrograms of organic residue. In contrast, the irradiation of gases produces one gram of tholins within 30 to 100 hours depending on the gas mixture (Sciamma-O'Brien *et al.*, 2010). Consequently, we chose to produce the tholins in the gas phase, using the

PAMPRE setup. A detailed description of this experimental setup can be found in (Gautier *et al.*, 2011; Szopa *et al.*, 2006). The reactor consists of a cylindrical stainless steel chamber where a radiofrequency capacitively coupled plasma (RF-CCP) is established in the gas mixture, between two electrodes. The gas mixture is injected as a continuous flow of 55 standard cubic centimeters per minute (sccm) through the polarized electrode and extracted by a vacuum pump. The chemistry forming the solid particles of tholins takes place between the electrodes which maintain the charged particles in levitation in the gas phase. When the weight of the particles exceeds a certain value, the particles fall into a vessel for later collection. This configuration allows the production of a large quantity of tholins.

The tholins were produced at an incident power of 30W and from a gaseous mixture of 95% nitrogen N₂ and 5% methane CH₄, representative of the main composition of Titan's atmosphere. The choice of this material was motivated by the fact that it has been physically and chemically characterized by a large number of previous studies (Carrasco *et al.*, 2009; Hadamcik *et al.*, 2013; Mahjoub *et al.*, 2012; Pernot *et al.*, 2010; Quirico *et al.*, 2008; Sciamma-O'Brien *et al.*, 2012). Moreover, those tholins were shown by Bonnet *et al.* (2015) as interesting precursors to simulate cometary N-rich refractory organics (before thermal heating). Titan tholins are made of a complex mixture of molecular and macromolecular material, partly heteropolymer-like, containing carbon, hydrogen and nitrogen atoms (Carrasco *et al.*, 2009; Pernot *et al.*, 2010). NMR, infrared and UV-Raman analyses showed the presence of aliphatic hydrocarbons, nitriles, imines, amines or N-bearing aromatic structures (Bernard *et al.*, 2006; Imanaka *et al.*, 2004; Quirico *et al.*, 2008), with unsaturations mainly involving nitrogen atoms (Carrasco *et al.*, 2009; Derenne *et al.*, 2008).

The optical properties of the Titan tholins produced with PAMPRE have been extensively characterized (Hadamcik *et al.*, 2013; Mahjoub *et al.*, 2012; Sciamma-O'Brien *et al.*, 2012). Mahjoub *et al.* (2012) measured the optical indices of tholins produced in the same conditions as in the present study. The real and imaginary parts of the refractive index, n and k , of the PAMPRE tholin thin film produced from a gas mixture of 95% N₂ and 5% CH₄ are provided from 370 to 1000 nm in the Table A1 of Mahjoub *et al.* (2012). The bidirectionnal reflectance spectra of PAMPRE Titan tholins have been presented in Figure 4 of de Bergh *et al.* (2008). They exhibit a strong red slope from 0.2 to 1.0 μm . This red slope was initially attributed to aromatic species present in the tholins structure (Imanaka *et al.*, 2004), but more recent work exclude the presence of large polyaromatic compounds in tholins (Quirico *et al.*,

2008) and favours the role of $n \rightarrow \sigma^*$ transitions of amine groups ($-\text{NH}_2$), known to be relatively intense from the UV to the visible range (Mahjoub *et al.*, 2012).

2.2.2 Water ice and mixture types

While it is clear that mixtures of water ice and organics are ubiquitous on icy surfaces in the Solar System, the way they are mixed together will depend on the history of the processes that have affected each particular surface. For comets, many different scenarios have been proposed to explain their formation and how the dust and the ice are mixed together (Belton *et al.*, 2007; Gombosi and Houppis, 1986; Greenberg, 1998; Greenberg and Li, 1999; Weissman, 1986).

In order to obtain reference laboratory data that could apply to diverse surface types and history, we have prepared two types of mixtures:

- (1) an **intra-mixture**, in which the tholins are thoroughly mixed with water inside each spherical ice particles constituting the sample (tholins are present as inclusions within water ice grains),
- (2) an **inter-mixture**, in which the tholins are deposited as a coating around the pure water ice particles.

Two water ice particle sizes were produced to investigate the influence of the water ice particles size on the sublimation: $67 \pm 31 \mu\text{m}$ and $4.5 \pm 2.5 \mu\text{m}$ diameters, respectively named **L** (for large) and **S** (for small) in the following. The L particles were compatible with both intra- and inter- mixtures, but the S particles could only be produced in the inter-mixture case. These led to three types of samples to be investigated: “**intra-mixture-L sample**”, “**inter-mixture-L sample**” and “**inter-mixture-S sample**”.

For all the samples, the mass ratio of organics to water was of 0.001 (0.1 wt.%). This mass ratio was dictated by the limited amount of tholins available. Although it may be very small compared to the natural mass ratio that could be found in icy extraterrestrial environments (this mass ratio of comet nuclei is expected to be ~ 1), it was sufficient to colour the ice and clearly observe the formation of sublimation lag deposits. Thus this gives a lower boundary on the existence of processes and the effect of tholins on the ice spectra.

The water ice particles were produced with the SPIPA (Setup for the Production of Icy Planetary analogs) setup developed in the LOSSy laboratory (Jost *et al.*, submitted).

The small (S) diameter water ice particles (Figure 1a) were produced following the method described in Pommerol *et al.* (2015a) and Jost *et al.* (submitted). An ultrasonic nebulizer (Hippomed AIR ONE) produces water droplets in the size range of 0.47 to 6 μm in diameter. The nebula is conducted through a plastic tube inside a freezer. The extremity of this pipe is held a few centimetres above a vessel made of stainless steel and cooled from below by a thick piece of copper plunging into a Dewar of liquid nitrogen. The small droplets of liquid water freeze instantly on contact with the air at -60°C and most of them sediment to the bottom of the vessel where they are kept at very low temperature around -120°C , limiting thermal metamorphism. The spherical shape of the ice particles and their size distribution were characterized by cryogenic scanning electron microscopy obtained at CSEM (Neuchatel). The ice particles produced via this method have a diameter of $4.5 \pm 2.5 \mu\text{m}$ (see Figure 1a).

The production of the larger water ice particles (Figure 1b) was performed using a different ultrasonic nebulizer which allows the preparation of ice particles made of an intra-mixture of water and tholins. Beforehand, a suspension of 0.1 wt.% tholins in liquid water was prepared by ultrasonication of 57 mg of tholins in 60 mL of distilled water. This ultrasonication enables the solubilization of the water-soluble molecules of the tholins (solubility 0.2 mg/mL in water, Carrasco *et al.*, 2009) and the homogenous suspension of the non-soluble molecules. It was performed with a Hielscher 200Ht ultrasonic unit equipped with a 7 mm diameter sonotrode. The ultrasounds were delivered in the liquid at the maximum amplitude of the sonotrode by steps of 0.5 seconds. The duration of ultrasonication was limited to 1 minute and the temperature of the suspension increased from 23°C to no more than 30°C . The obtained homogenous suspension was then allowed to cool down to room temperature while maintained in motion with a magnetic stirrer. Then, the solution of pure water or the suspension of 0.1% tholins in water was put in a spray bottle equipped with a 2 mm diameter tube connected to a Hielscher 200Ht ultrasonic unit equipped with a S26d18S sonotrode for spraying and nebulizing. The liquid pumped from the bottle was injected into the sonotrode and spread out as a thin film on the conical shaped nozzle surface at the output of the sonotrode. The ultrasonic vibrations delivered to the sonotrode nozzle disintegrate the liquid into micro-droplets. This nebulization takes place inside the freezer, above a stainless steel vessel filled with liquid nitrogen. The droplets ejected by the sonotrode

nozzle fall into the liquid nitrogen where they instantly freeze into ice particles. The ice particles produced by this method are spherical and have a diameter of $67\pm31\mu\text{m}$ as measured by cryo-SEM (see Figure 1b).

The inter-mixture samples were prepared by weighing 55 g of water ice particles in an aluminium bottle, followed by the addition of 60 mg of tholins. The bottle was then closed and agitated using a Vortex-Genie2 mixer at full speed for 15 seconds and repeated 3 times. During the weighing and the vortexing, the aluminium bottle was repeatedly plunged into liquid nitrogen to ensure the preservation of the ice particles at very low temperature so as to limit thermal metamorphism.

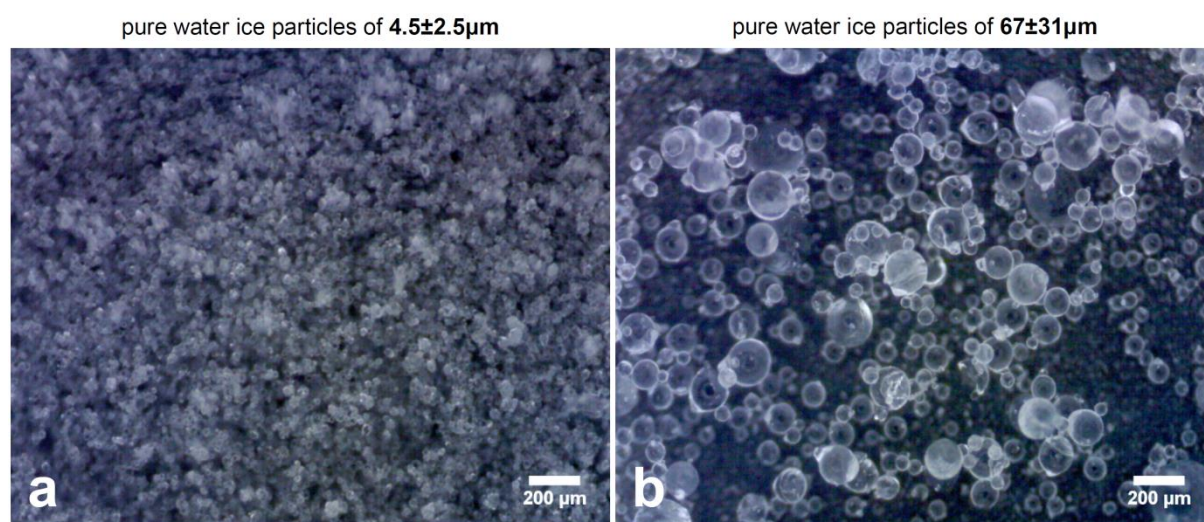


Figure 1: Optical microscope images of pure water ice particles prepared with the Setup for the Production of Icy Planetary analogs (SPIPA). **(a)** Small "S" size water ice particles ($4.5\pm2.5\mu\text{m}$), agglomerates of several tens of micrometers and **(b)** Large "L" size water ice particles ($67\pm31\mu\text{m}$). (For a colour version of this figure, the reader is referred to the web version of this article)

2.2.3 Deposition of the ice samples into the sample holder

Two simulation experiments were conducted inside the SCITEAS chamber on a total of 4 samples. For each experiment, a rectangular $120\times60\text{ mm}$ sample holder 20 mm thick was divided in two equal compartments and each compartment was filled with a different ice sample. This enables to compare the evolution of different ice mixtures exposed to the same

pressure and temperature conditions over the whole simulation. The sample holder was also equipped with 3 temperature sensors fixed at various places: one was directly glued at the bottom of the sample compartment and the other two were positioned in order to measure the temperature inside and outside the ice samples. Prior to the deposition of the ice samples, the sample holder was cooled at around -100°C. The sample deposition described below took place in a freezer, followed by a rapid transfer of the sample in the SCITEAS chamber.

For experiment n°1, the sample holder was filled with the “**intra-mixture-L sample**” on the one side, and with the same size ice particles made of pure water on the other side. Both samples were deposited in the form of a suspension of ice particles and liquid nitrogen. The evaporation of the liquid nitrogen in contact with the sample holder leads to the formation of bubbles and holes inside the sample, as seen in Figure 3.

For experiment n°2, the sample holder was filled with the “**inter-mixture-L sample**” on the one side, and with the “**inter-mixture-S sample**” on the other side. The inter-mixture samples cannot be deposited using liquid nitrogen because it could alter the tholins coating of the particles. So these inter-mixture samples were deposited by direct sieving of the ice obtained after mixing using a 400 µm sieve. The sieving was necessary to avoid putting too big agglomerates of ice particles into the samples. This deposition method resulted in samples having a more homogenous surface, free of any hole, compared to the experiment n°1 (see Figure 3).

Experiment:	Experiment n°1		Experiment n°2	
Sample name:	pure water ice-L	intra-mixture-L	inter-mixture-L	inter-mixture-S
Tholins/water mass ratio:	0	0.001	0.001	0.001
Mixture type:	N.A.	intra-mixture	inter-mixture	inter-mixture
Ice particle size (µm):	67±31	67±31	67±31	4.5±2.5
Density (g cm ⁻³) :	0.5	0.5	0.5	0.3

Table 1: Characterization of the prepared tholins-ice samples. Each sample is designated by its abbreviated "Sample name" in the text and in the Figures.

2.3 Simulation sequence in the SCITEAS chamber

2.3.1 Experimental conditions: pressure and temperature profiles

Directly after preparation, the sample holder and the internal calibration target were transferred into the SCITEAS chamber. The temperature sensors were connected and the chamber was hermetically closed. The cooling of the chamber immediately started and the primary and turbo-molecular pumps were progressively started (see for details Pommerol *et al.*, 2015a).

The profiles of pressure and sample holder temperature through the entire experiment are presented on Figure 2. The experiment n°1 lasted for 45 hours while the experiment n°2 only ran for 13 hours. For both experiments, two hours after the closing of the chamber, the temperature of the shroud was at around -180°C and the sample holder at around -100°C. The pressure inside the chamber was about 2.10^{-5} mbar. The temperature profiles of the sample holder show a continuous and logarithmic-shaped increase from -100°C to about -70°C after more than 42 hours.

Over the duration of the experiments, the pressure was most of the time comprised between 1.10^{-5} and 2.10^{-5} mbar. The pressure curve in Figure 2 shows bumps from 0 to 10 hours, which originate from the sublimation and re-deposition of water frost from the sample holder structure to the cold shroud surrounding the chamber. Shorter variations of pressure are also seen over the whole time lapse. These pressure spikes have typical durations of a few minutes only. Some of these spikes can be correlated with events affecting the surface of the samples as discussed in section 3.1.

Overall, the temperature and pressure variations were very similar for experiments n°1, n°2 as for the reference experiment "comet #1" described in Pommerol *et al.* (2015a).

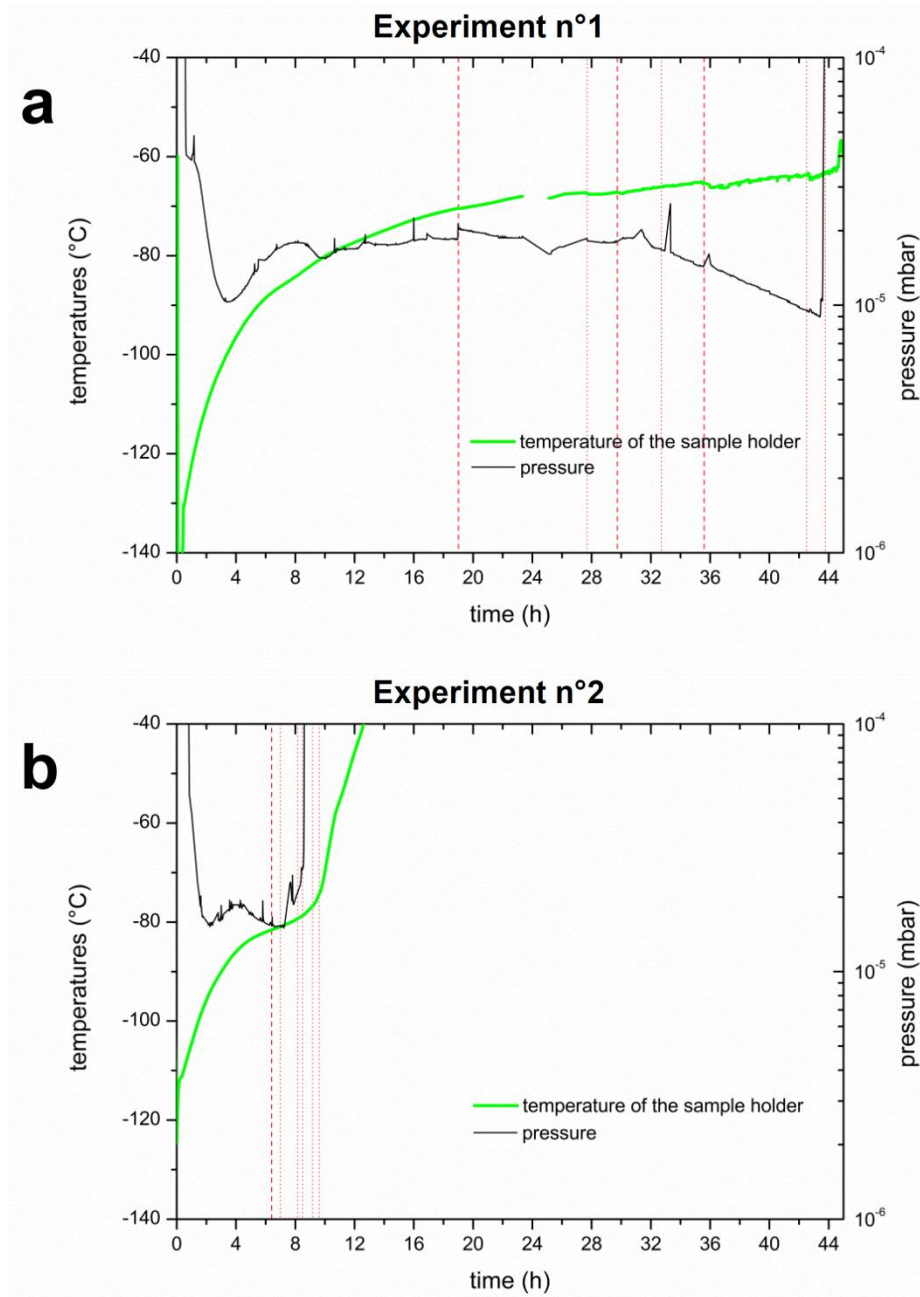


Figure 2: Temperature and pressure conditions measured inside the SCITEAS chamber during the experiments n°1 **(a)** and n°2 **(b)**. Vertical red bars indicate the time during which an ejection event occurred on the samples (as listed in section 3.1). Dashed lines indicate events that can be correlated to a pressure increase or spike. Dotted lines indicate events that cannot be clearly correlated to a pressure variation. (For interpretation of the references to colour in this figure legend, the reader is referred to the web version of this article)

2.3.2 Dataset description

The dataset acquisition was similar for experiments n°1, n°2 and reference experiment "comet#1" presented in details in Pommerol *et al.* (2015a).

The acquisition of visible images of the sample started just after the connection of the last temperature sensor, a few seconds before closing the SCITEAS chamber. One image was taken every minute with the ambient light of the laboratory (white mercury-vapour fluorescent tubes) turned on. These images document the evolution of the sample surface during periods when the ambient light is turned on but they cannot be used for accurate photometric studies.

About 2 hours after the start of each experiment, the ambient light of the laboratory was turned off and the long-term spectro-photometric measurements sequence started. Monochromatic images at 600 nm (providing the best dynamic range) were acquired every minute and hyperspectral cubes were measured every 40 minutes. When the light of the laboratory was intermittently turned on again for visual inspection of the experiment, the spectro-photometric measurements were interrupted and only visible images were acquired.

Black and white monochromatic images at 600 nm and visible images taken with the ambient light on were assembled to create Video 1 and 2, depicting the evolution of the samples for experiment n°1 and n°2 respectively. Colour composites were produced from the monochromatic images acquired using the visible CCD (Figure 3). All colour composites were assembled to create a Video 3 and Video 4 depicting the evolution of the samples for experiment n°1 and n°2 respectively.

3. Results

3.1 Evolution of the surface morphology

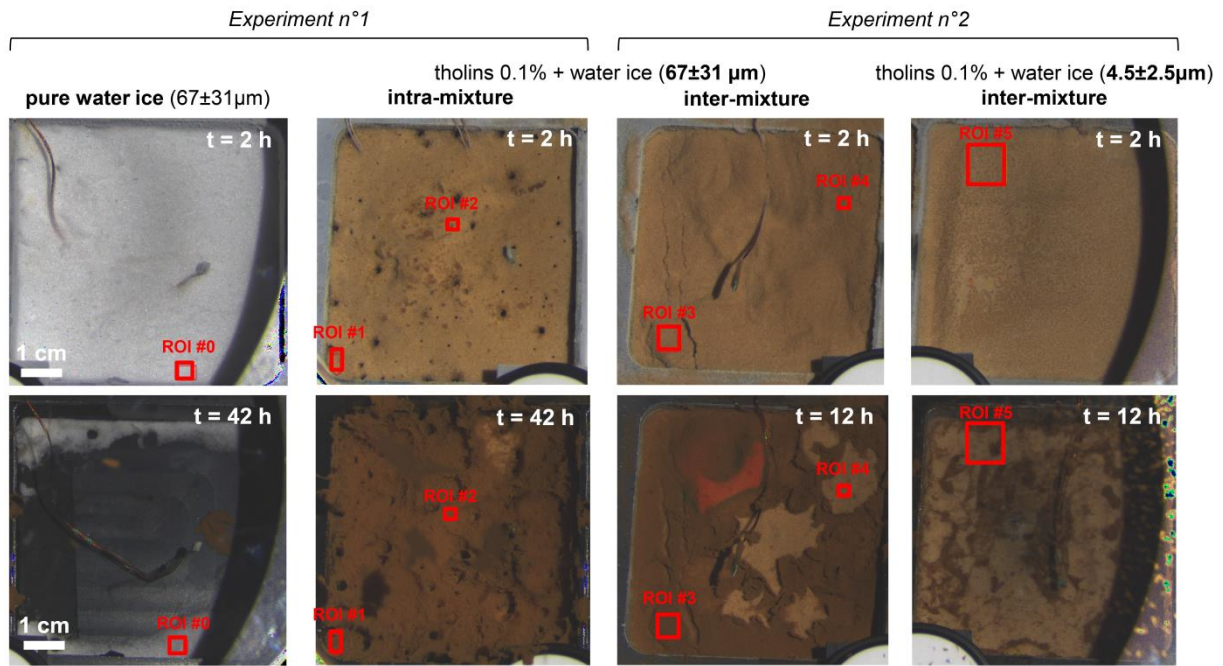
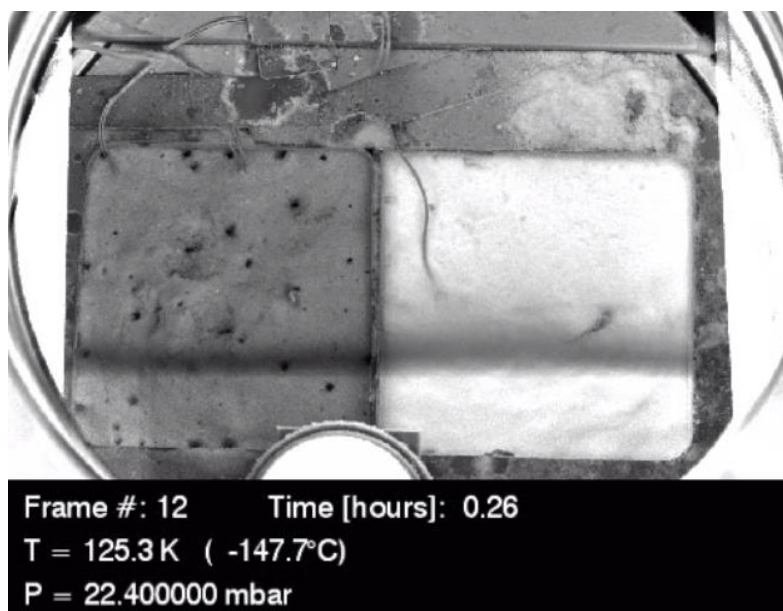


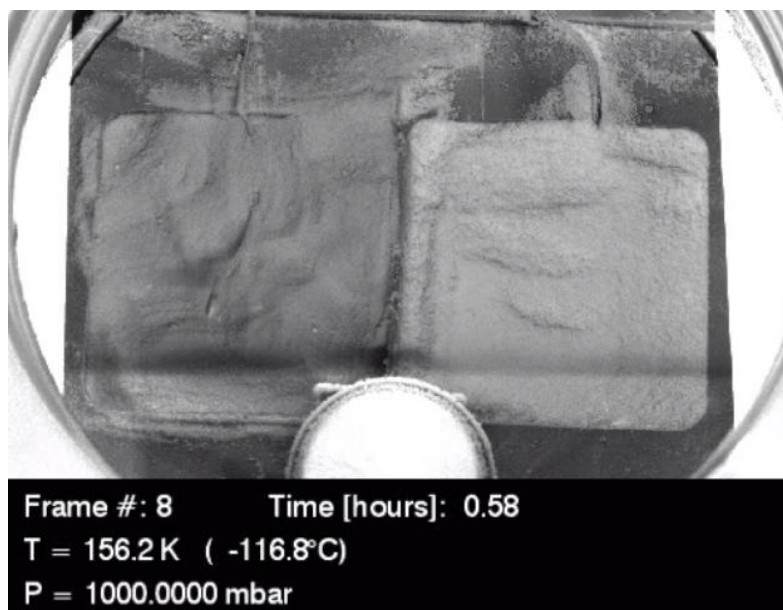
Figure 3: Colour composites showing the surface of each sample 2 hours after the beginning of the simulation and at the end, 40 or 10 hours later. One should appreciate the diversity of morphologies produced by the sublimation process just by changing the mixture type or the ice particle sizes. The Regions Of Interest (ROI) indicated in each image have been used to retrieve the spectro-photometric data presented in Figure 6, Figure 7 and Figure 8. ROIs #2, #4 and #5 were chosen because these areas are affected by events of ejection of sublimation mantle, while in ROIs #1 and #3 the mantle is progressively deposited onto the ice surface without ejection event (see Videos 3, 4). The VIS image appears close to natural colours, relatively similar to what the human eye would see, although no special calibration was performed to retrieve the true colours. For the VIS colour composite, monochrome images acquired at 0.40, 0.52, and 0.60 μm are used, for the blue, green, and red channel, respectively. Videos 3 and 4 show all the colour composites separating each of these two images. (For a colour version of this figure, the reader is referred to the web version of this article)

Figure 3 shows visible colour composites of the studied samples, showing the evolution of their surfaces from t = 2 h to the end of the simulation. Moreover, the pictures

acquired every minutes from $t = 0$ h to the end using the visible camera were assembled to create a video depicting the evolution of the samples during the 45 hours of the experiment n°1 (Video 1) and the 13 hours of experiment n°2 (Video 2). A detailed analysis of these videos is provided in the Supplementary Material, and is briefly summarized below.



Video 1: This black and white video shows the evolution of the samples during the experiment n°1. From left to right are the samples **tholins intra-mixture-L** and **pure water ice-L** (see Table 1). Both monochromatic images at $0.60\ \mu\text{m}$ and visible images taken with the ambient light on have been put together in this video (see sections 2.1 and 2.3.2 for details). The temperature of the sample holder and the pressure inside the chamber are indicated on each frame (see also Figure 2). A detailed analysis of the events occurring during this video is provided in section 3.1.1.



Video 2: This black and white video shows the evolution of the samples during the experiment n°2. From left to right are the samples **tholins inter-mixture-L** and **tholins inter-mixture-S** (see Table 1). Both monochromatic images at 0.60 μm and visible images taken with the ambient light on have been put together in this video (see sections 2.1 and 2.3.2 for details). The temperature of the sample holder and the pressure inside the chamber are indicated on each frame (see also Figure 2). A detailed analysis of the events occurring during this video is provided in section 3.1.2.

3.1.1 Build-up of mantles or aggregates at the surface of the ice during sublimation

Evolution of the intra-mixture-L and inter-mixture-L samples: During the first hours of sublimation, the surface of the samples gets darker. As the water ice sublimates, a deposit made of the non-volatiles compounds initially present in the ice builds up at the surface of the samples, causing changes of colour and texture. This deposit is designated as the “sublimation mantle” or the “sublimation lag deposit” in the following paragraphs. Starting at about 6 h (for the inter-mixture-L) and 19 h (for the intra-mixture-L), sudden releases of fragments of sublimation mantle occur, designated as “ejection events”. The areas from where the material is released appear brighter on the visible images. This bright material is made of the mixture of water ice and tholins, initially located below the sublimation mantle, which is now exposed to the top of the sample, as confirmed by the near infrared spectra (see Figure 7). Some of these ejection events are correlated to an increase of pressure in the chamber of the order of

10^{-6} mbar (see the red dashed lines in Figure 2). Several minutes after each ejection event, the bright areas of exposed ice become darker as the ice sublimates, rebuilding the tholins mantle. On the intra-mixture-L sample, some ejection events release more than 50% of the total surface of the sample; whereas on the inter-mixture-L, they always represent less than 10% of the surface of the sample (see Figure 3). The mantle fragments ejected by the inter-mixture-L sample are similar to a skin just 1 or 2 mm thick, which looks more compact than the very fluffy mantle obtained by sublimation of the intra-mixture-L sample (see Figure 3 and Figure 4a,b).

Evolution of the inter-mixture-S sample: After few minutes of sublimation, the surface of the sample gets speckled, covered by numerous dark dots smaller than 1mm. After few hours, the small dark dots are concentrically ejected from the left centre of the sample. Some tholins accumulate all around the rim of the sample holder, and later these aggregates of tholins migrate back toward the centre of the sample. Some aggregates grow in size by the accumulation of tholins and others are ejected by the gas flow. The surface is much more dynamic than for the two other samples (see Supplementary Material for more details).

3.1.2 Morphology and physical properties of the sublimation lag deposits

Figure 4 and Figure 5 show high-resolution images of the sublimation residues obtained at the surface of each sample.

The Figure 4a shows the surface of the intra-mixture-L sample after 43 hours of sublimation. The multiple dark hollows seen on this image are remnants of the channels created in the ice sample by the evaporation of the liquid nitrogen during the deposition in the sample holder (see Figure 3 and section 2.2.3). Between these hollows, the tholins expelled from the ice particles after the sublimation of the water have merged into filaments forming a three dimensional network, corresponding to the sublimation mantle, over the ice particles (see also Figure 5b). The ice particles are mostly not visible in Figure 4a, except in a small area on the left side (indicated by an arrow) where a fragment of the mantle has recently been ejected. As seen in Video 1, some fibres of this network are locally vibrating and the whole mantle is inflated by the flow of water vapour produced by the sublimation of the water ice particles located below the mantle. Knowing the thickness of the sample and its concentration in tholins, the density of this inflated mantle is estimated to be around $5 \cdot 10^{-4}$ g cm⁻³, and its

porosity is likely to be around 90% (the initial density of the ice sample was around 0.5 g cm^{-3}). Some materials are known to reach such high porosity, for example ceramics (Ozgür Engin and Tas, 1999) or foam made of organic polymers (Meador *et al.*, 2012).

Figure 4b presents the surface of the inter-mixture-L sample after 13 hours of sublimation inside the chamber. The tholins deposited at the surface after the sublimation of the ice particles form a 1 to 2 mm mantle resembling a thick “skin” on top of the sample. Similarly to the intra-mixture-L sample, this tholins deposit also consists of a network of filaments (seen at higher resolution in Figure 5b) but these filaments are more loosely connected to the water ice particles located beneath it. Several fragments of the mantle in Figure 4b appear “unstuck” to the ice surface.

Finally, the Figure 4c shows the surface of the inter-mixture-S sample after 13 hours of sublimation. Here the tholins do not form a relatively continuous mantle over the ice but are rather accumulated locally as 2 to 3 mm aggregates. Over the ice surface, between the aggregates, very loose filaments are seen (seen on Figure 4c and at higher resolution in Figure 5a). Those are continuously ejected from the surface, as seen in Video 2 and Video 4.

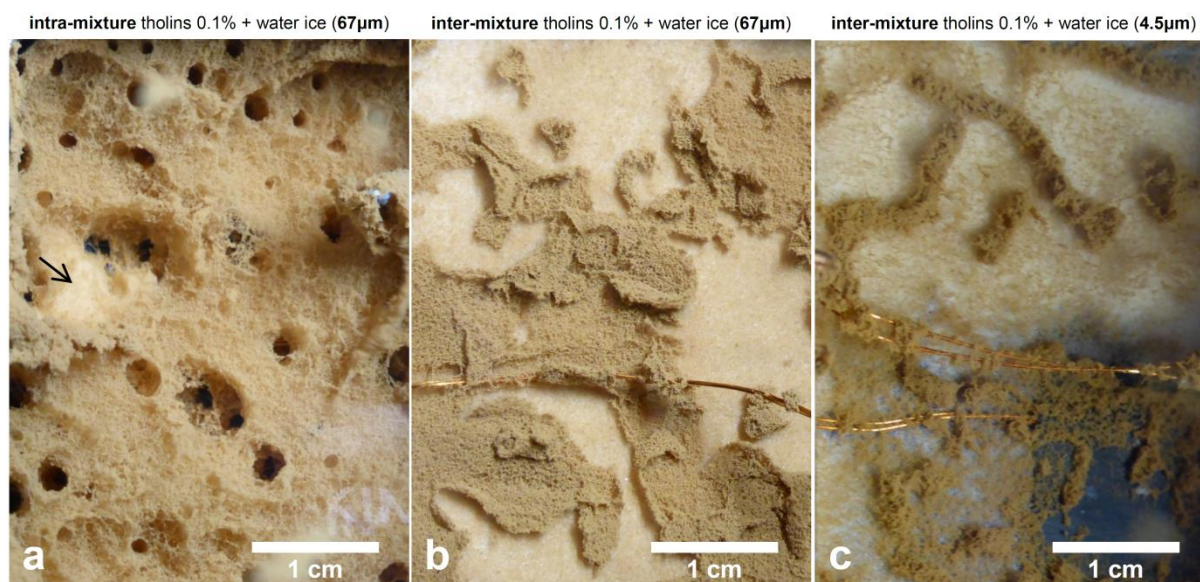


Figure 4: High resolution images of the sample surfaces after sublimation. (a) intra-mixture of 0.1% tholins and water ice particles of $67 \pm 31 \text{ } \mu\text{m}$, (b) inter-mixture of 0.1% tholins and pure water ice particles of $67 \pm 31 \text{ } \mu\text{m}$, (c) inter-mixture of 0.1% tholins and pure water ice particles of $4.5 \pm 2.5 \text{ } \mu\text{m}$. These images were taken *in situ*, around the end of the experiments,

while the samples were sublimating inside the SCITEAS chamber. The arrow on Figure (a) indicates an area where an ejection of mantle fragment occurred and where ice particles have been consecutively exposed to the surface. This area appears brighter than the surrounding. Such areas are also clearly seen in Figures (b) and (c). (For a colour version of this figure, the reader is referred to the web version of this article)

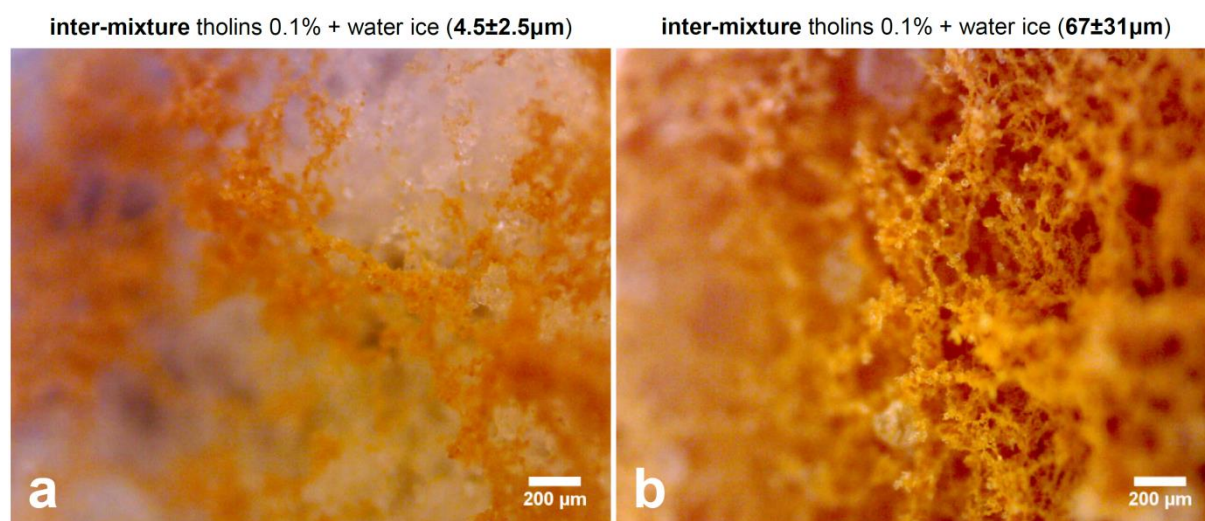


Figure 5: Optical microscope images of the sublimation residues of (a) inter-mixture of 0.1% tholins and pure water ice particles of $4.5 \pm 2.5 \mu\text{m}$, (b) inter-mixture of 0.1% tholins and pure water ice particles of $67 \pm 31 \mu\text{m}$. The thinner filaments seen in (b) are of the order of $1 \mu\text{m}$ thick, most are around $10\text{-}15 \mu\text{m}$ thick, and bigger agglomerates are up to $30 \mu\text{m}$. Some deposition of water frost are seen in (b), but the filamentous matrix was free of any water ice after the end of the experiments (this water frost comes from the condensation of some water vapor from the atmosphere of the laboratory). (For a colour version of this figure, the reader is referred to the web version of this article)

3.1.3 Texture of the remaining ice after the experiments

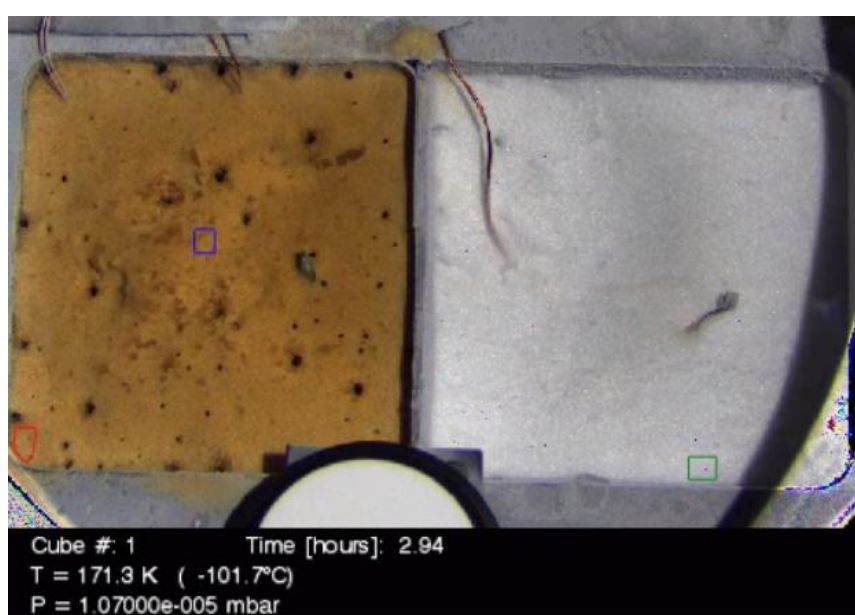
At the end of the experiments n°1 and n°2, the samples were removed from the SCITEAS chamber and their textures were probed using a steel spatula. The ice particles of the intra-mixture-L sample appear to be slightly consolidated just below the sublimation deposit, and have a fluid texture similar to the initial sample below this thin crust of ice. However, the ice particles of the inter-mixture-L sample have lost their initial fluidity: they

appear to be strongly consolidated at all depths. This consolidation probably comes from the re-condensation of the water between the ice particles, building bonds that connect the ice particles together and provide solidification of the whole sample. The texture of the ice of the inter-mixture-S sample seems to be unchanged, according to the qualitative diagnosis used here. We plan to quantify the compressive strengths of these ice samples with a dedicated device for our future experiments. The fact that a significant reconsolidation occurs only for the inter-mixture-L sample is probably related to the initial mixture type (presence of non-volatiles between the individual ice particles) and/or to the specific texture of the sublimation mantle produced during sublimation.

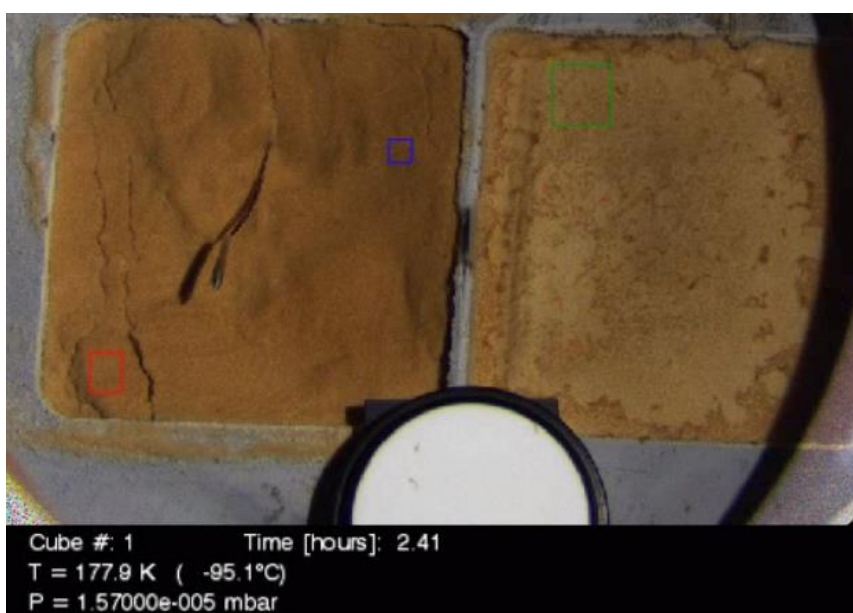
The hypotheses concerning mechanisms of the mantle building, ice hardening and ejection events are developed in the discussion sections of this article (sections 4.1 and 4.2).

3.2 Evolution of the spectro-photometric properties of the samples

The spectro-photometric characteristics of the samples surfaces are studied as a function of time through the detailed analysis of the hyperspectral cubes acquired during the experiments. Figure 6, Figure 7 and Figure 8 present a subset of the hyperspectral data acquired with the imaging spectrometer and Video 3 and Video 4 depict the evolution of the samples for experiment n°1 and n°2 respectively.



Video 3: This colour video shows the evolution of the samples during the experiment n°1. From left to right are the samples **tholins intra-mixture-L** and **pure water ice-L** (see Table 1). Each image of this video is a colour composite of three monochrome images acquired at 0.40, 0.52, and 0.60 μm , for the blue, green, and red channel, respectively (see sections 2.1 and 2.3.2 for details). The temperature of the sample holder and the pressure inside the chamber are indicated on each frame (see also Figure 2). The Regions Of Interest (ROI) indicated in each frame have been used to retrieve the spectro-photometric data presented in Figure 6, Figure 7 and Figure 8 (red = ROI #1, blue = ROI #2, green = ROI #0).



Video 4: This colour video shows the evolution of the samples during the experiment n°2. From left to right are the samples **tholins inter-mixture-L** and **tholins inter-mixture-S** (see Table 1). Each image of this video is a colour composite of three monochrome images acquired at 0.40, 0.52, and 0.60 μm , for the blue, green, and red channel, respectively (see sections 2.1 and 2.3.2 for details). The temperature of the sample holder and the pressure inside the chamber are indicated on each frame (see also Figure 2). The Regions Of Interest (ROI) indicated in each frame have been used to retrieve the spectro-photometric data presented in Figure 6, Figure 7 and Figure 8 (red = ROI #3, blue = ROI #4, green = ROI #5).

3.2.1 Comparison of the reflectance spectra before/after sublimation

Regions of Interest (ROIs): The reflectance of the samples surfaces was extracted from the hyperspectral images only at some limited areas, called Regions of Interest (ROIs), indicated in Figure 3. Extracting the average spectra of the whole samples surfaces was not possible because of the presence of external elements in the images: mainly fragments of sublimation mantle stuck on the window of the chamber hiding some parts of the sample and casting shadows on other parts, and temperature sensors and their shadows. The selection of limited ROI areas was done in order to characterize the spectral evolution of active versus inactive areas over the samples. To do this, ROIs #2, #4 and #5 were chosen because these areas are affected by events of ejection of sublimation mantle, while in ROIs #1 and #3 the mantle is progressively deposited onto the ice surface without ejection event (see Videos 3 and 4).

Figure 6 presents, for each water ice and tholins sample, the initial (black line) and final (red line) reflectance spectra averaged over the ROIs represented in Figure 3. To facilitate the interpretation of these spectra, reference spectra of pure water ice and pure tholins are also shown (reference spectra from our own experiments, measured with the SCITEAS imaging system). The initial reflectance spectra are characterized by a red slope from 0.4 μm to about 0.95 μm , due to the presence of tholins, followed by water ice absorption bands at 1.02, 1.26 and 1.51 μm . From 0.4 to 0.9 μm , the initial reflectance spectra are brighter than the pure tholins by 50% (at 0.8 μm) to 600% (at 0.4 μm). From 0.95 to 1.4 μm the tholins are brighter than the water ice and contribute to increase the reflectance of the sample by 20-30% or 2-7% compared to pure water ice of 70 μm or 5 μm diameter respectively. One should note that these initial reflectance spectra have been acquired about 2 hours after the start of each experiment, meaning that they do not show the reflectance of the pristine ice mixtures (this waiting time of 2 hours was necessary to make sure that the cooling system of the simulation chamber reaches a permanent stable regime). Indeed during these 2 hours in the chamber the samples started to evolve due to the sublimation of the water (see Video 1 and Video 2). Consequently, these initial reflectance spectra cannot be used to assess the influence of the mixture type (inter- or intra-, large or small ice particles) on the reflectance. The aim of the Figure 6 is rather to compare the reflectance of the samples before and after sublimation.

Most of the final reflectance spectra in Figure 6 (ROI #1, #3, #5 and #2) show lower reflectance in the visible range, due to the deposition of pure tholins on top of the samples (Figure 6f (ROI #0) shows that the reflectance of pure water ice also decreased, probably because of the accumulation of dust present in the water or because of the change of the size distribution of the surface ice grains after sublimation).

For ROI #1 (intra-mixture-L sample) and ROI #3 (inter-mixture-L sample), the 0.4-0.95 μm red slopes get the closest to that of the pure tholins because these ROIs accumulated thicker deposit of tholins than ROI #2 and ROI #4, on the same samples, which have undergone resurfacing events. In the near-infrared range, most of the samples exhibit a significant decrease of the depth of the water ice absorption bands, again more pronounced in ROI #1 and #3 but also in ROI #5 (inter-mixture-S sample). The bands at 1.02 and 1.26 μm have almost completely disappeared in the final reflectance spectrum of ROI #1 on the intra-mixture-L sample (Figure 6a), and the 1.02 μm band is hardly detectable in the final reflectance spectrum of ROI #5 on the inter-mixture-S sample (Figure 6c). Beyond around 1.2 μm , the sublimated surfaces of intra-mixture-L (ROI #1) and inter-mixture-L (ROI #3) samples are brighter than before sublimation because of the reduced absorption of the water bands but also because of the deposit of tholins which are relatively bright in the near infrared (Figure 6a and b). In contrast, the sublimated surface of the inter-mixture-S sample (ROI #5, Figure 6c) has a reflectance lower than before sublimation, probably because it is not covered by a thick layer of tholins compared to the other samples. Finally, it is interesting to notice that the reflectance spectrum of ROI #4 after 12 hours of sublimation is very similar to the one acquired before the start of the sublimation: this is because of an ejection event that occurred just before $t = 12\text{h}$ and cleaned the surface from the tholins dust mantle (see video 4).

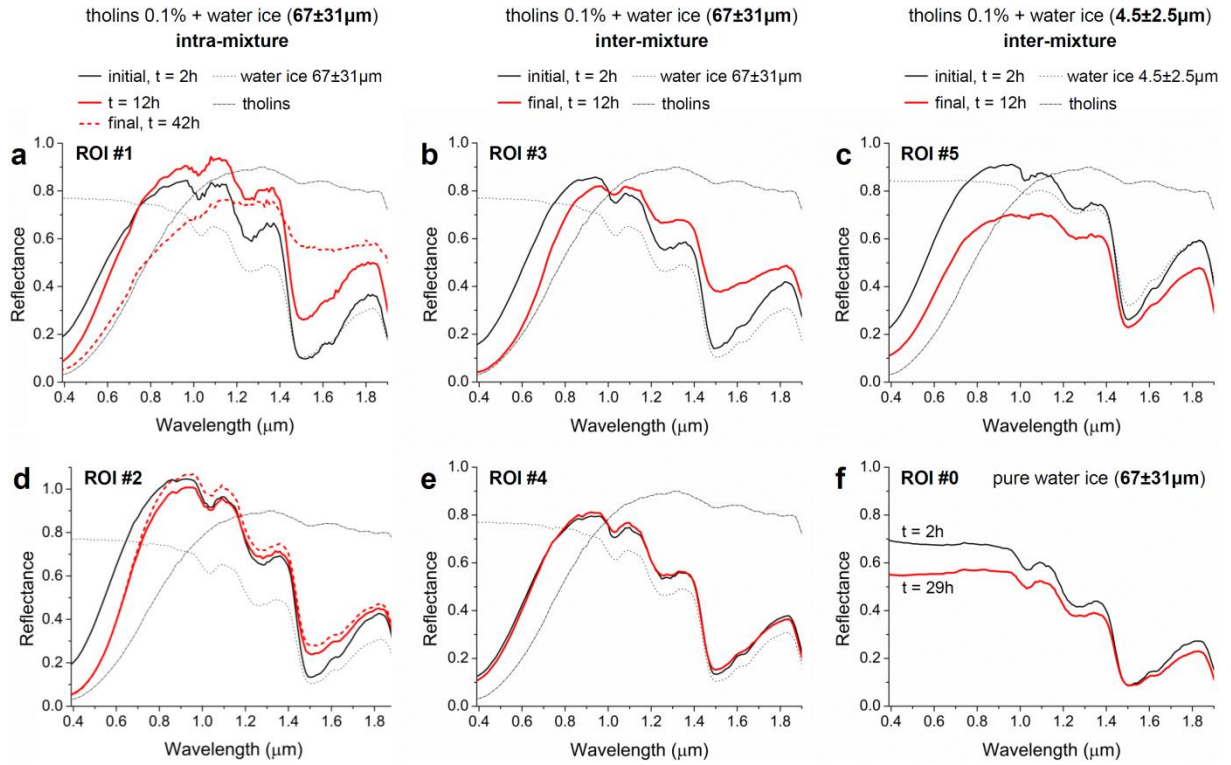


Figure 6: Reflectance spectra of the sample surfaces in the Regions of Interest (ROIs) indicated in Figure 3. The reflectance spectra measured two hours after the start of the simulation (black line) can be compared to the ones measured 40 or 10 hours later (red line). To facilitate the interpretation of these spectra, reference spectra of pure water ice and pure tholins are also shown in dotted and dashed lines respectively. ROIs #2, #4 and #5 are affected by events of ejection of sublimation mantle, while in ROIs #1 and #3 the mantle is progressively deposited onto the ice surface without ejection event (see Videos 3, 4 and Figure 7). A detailed interpretation of these spectra is provided in section 3.2. (For interpretation of the references to colour in this figure legend, the reader is referred to the web version of this article)

3.2.2 Comparison of the *in situ* spectral evolutions of the samples

The whole sequence of hyperspectral cubes acquired during the experiments allows to study the dynamic of the evolution of the samples' reflectance as the sublimation goes on.

The Figure 7 and Figure 8 compile the temporal evolution of several spectral data for all the ROIs of the three different water and tholins ice samples (see ROIs on Figure 3), presented on the same time axis. However, one should note that the temperature and pressure

conditions did not exactly follow the same temporal evolution for experiment n°1 and n°2 (see Figure 2). As a consequence, the direct comparison of the spectral evolutions seen on Figure 7 and Figure 8 must be done with caution. Figure 7 indicates the spectral evolution of ROIs where the mantle is progressively deposited onto the ice surface (without ejection event) (ROI #1 and #3) whereas the Figure 8 shows the evolution of ROIs affected by events of ejection of sublimation mantle (ROIs #2, #4 and #5).

The spectral data plotted in Figure 7 and Figure 8 are:

- (a) the reflectance at 0.40 μm , located in the tholins absorption band,
- (b) the normalized spectral red slope between 0.40 and 0.94 μm due to the tholins (following the definition from Fornasier et al., 2015):

$$\text{Spectral Red Slope (\%/100 nm)} = \frac{R_{0.94\mu\text{m}} - R_{0.40\mu\text{m}}}{(940 - 400) \times R_{0.40\mu\text{m}}} \times 10^4 \quad \text{Eq. (1)}$$

- (c) and the band depth of the water absorption band centered at 1.51 μm :

$$\text{Water band depth at 1.51 } \mu\text{m} = 1 - \frac{R_{1.51\mu\text{m}}}{R_{1.35\mu\text{m}}} \quad \text{Eq. (2)}$$

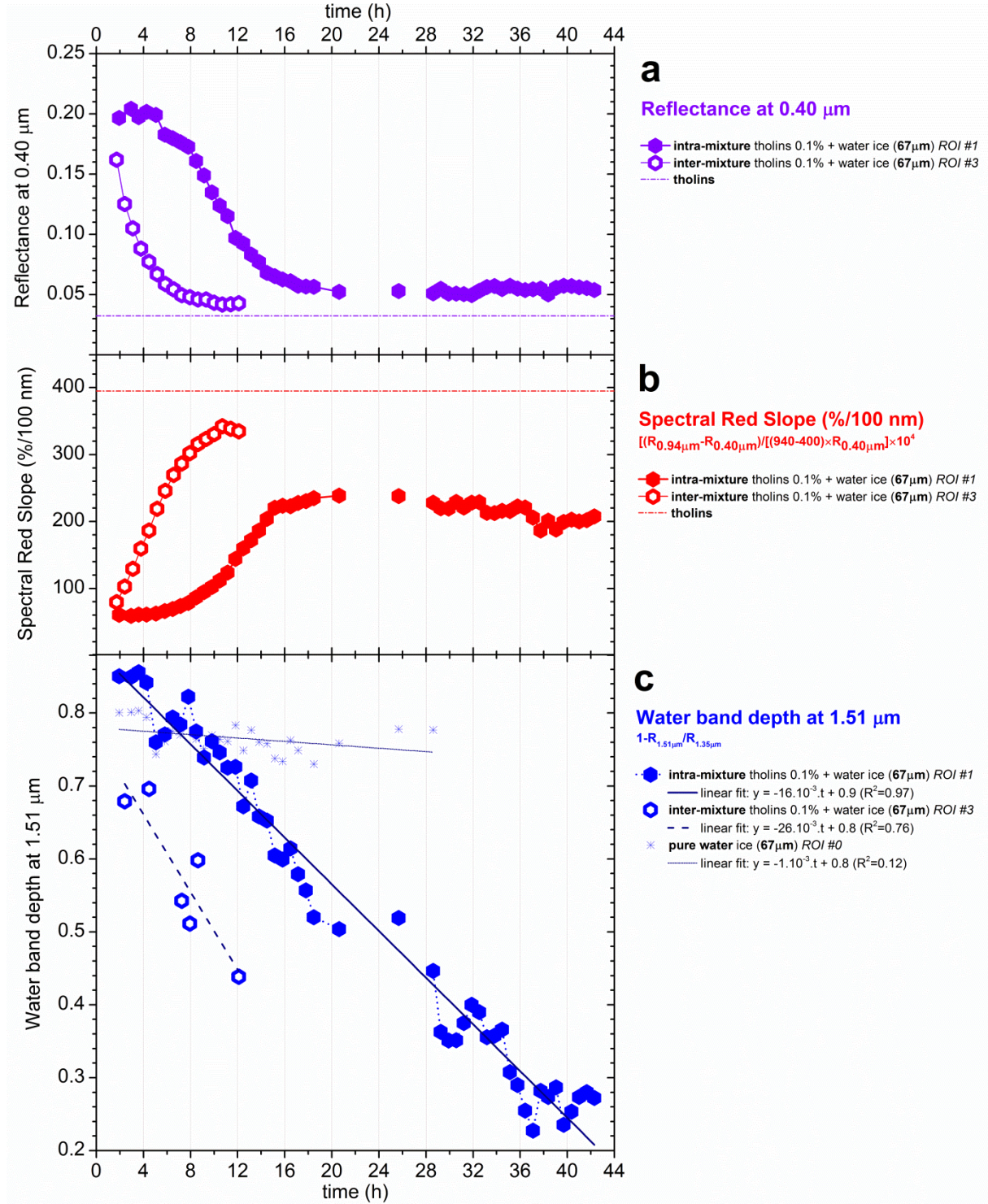


Figure 7: Spectral evolution of areas where the sublimation mantle is progressively deposited on top of the ice (no ejection event) (ROI #0, ROI #1, ROI #3 can be located in Figure 3). Temporal evolution of (a) the reflectance at 0.40 μm where tholins absorb the most, (b) the normalized spectral red slope due to tholins between 0.40 and 0.94 μm (see Eq. 1), (c) the band depth of the water absorption band at 1.51 μm (see Eq. 2). ROI #1 is located in a corner of the sample holder, very close to the walls, so that its temperature (and consequently its

sublimation rate) is lower than the other ROIs located farther away from the walls. Consequently, for a more reliable comparison of the trends of the spectral properties of intra-mixture-L sample with the other samples, the reader is invited to look at Figure 8, in which all the presented ROIs are farther from the walls. (For a colour version of this figure, the reader is referred to the web version of this article)

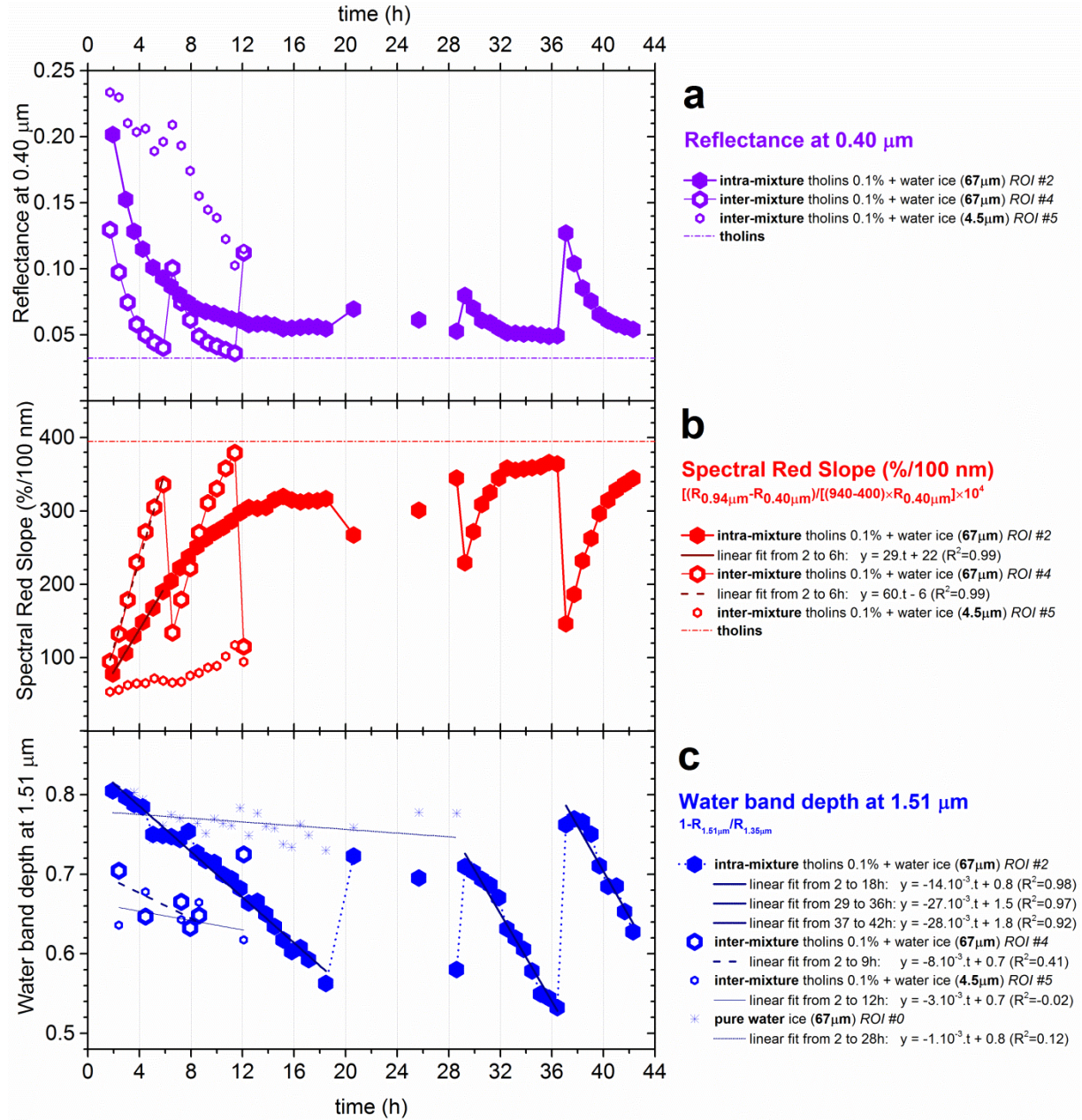


Figure 8: Spectral evolution of areas where ejection events occurred at the surface of the samples (ROI #0, ROI #2, ROI #4 and ROI #5 can be located in Figure 3). Temporal evolution of (a) the reflectance at 0.40 μm where tholins absorb the most, (b) the normalized

spectral red slope due to tholins between 0.40 and 0.94 μm (see Eq. 1), (c) the band depth of the water absorption band at 1.51 μm (see Eq. 2). (For a colour version of this figure, the reader is referred to the web version of this article)

3.2.2.1 Long term spectral evolution

Reflectance at 0.40 μm and spectral red slope: As the water sublimates, the reflectance at 0.40 μm decreases for all samples because of the deposition of water-free tholins over the surface (Figure 7a and Figure 8a). From all the regions of interest, the ROI #1 (Figure 7a) on the intra-mixture-L sample exhibits the slowest decrease and follows a sigmoidal curve. This peculiar behavior is due to the very special location of ROI #1, in the very corner of the sample holder (see Figure 3), in which the sublimation rate is lower than at the center of the sample holder. Indeed, on the same sample, ROI #2, which is more centered, shows a faster decrease of reflectance following an exponential-shaped curve (see Figure 8a). So apart for very special locations on the samples, both inter- and intra- mixtures-L samples, exhibit a decrease of reflectance following exponential-shaped curves and having for asymptote the reflectance value of pure tholins (dotted-dashed lines in Figure 7a and Figure 8a). When comparing ROI #2 and ROI #4 (Figure 8a), the decrease observed is significantly slower for the intra-mixture than for the inter-mixture: the reflectance at 0.40 μm decreased by 70% in 4 hours for the inter-mixture-L sample (ROI #4), whereas 9.5 hours were needed for the reflectance of the intra-mixture-L sample (ROI #2) to decrease by the same amount. Moreover, the inter-mixture-L sample reaches a reflectance value at 0.40 μm close to that of pure tholins ($R_{\text{tholins}}+10\%$) in few hours whereas the intra-mixture-L sample never reaches a reflectance less than $R_{\text{tholins}}+50\%$ after more than 42 hours of sublimation (see Figure 7a and Figure 8a).

For all samples, the spectral red slope between 0.40 and 0.94 μm , plotted in Figure 7b and Figure 8b, follows the exact opposite variations than the reflectance at 0.40 μm , plotted in Figure 7a and Figure 8a. As the tholins accumulate at the surface of the sample, the absorption of the surface at 0.40 μm increases, and consequently the reflectance at 0.40 μm decreases and the spectral red slope increases. During the first 4 hours of sublimation (from $t=2\text{h}$ to $t=6\text{h}$), the spectral slope of the inter-mixture-L sample (ROI #3) increases about two times faster than for the intra-mixture-L sample (ROI #1) (Figure 8b). However, one must note that the average sublimation rate of the ice in the inter-mixture-L sample (0.12 mm/h) is

about two times lower than in the intra-mixture-L sample (0.20 mm/h) (see Table 2). This suggests that the sublimation mantle formed on the inter-mixture-L sample must be denser than the one of the intra-mixture-L sample to account for the faster reddening. After this initial increase of the red slopes, a slowing down is observed and the red slopes reach a plateau equal to 87% and 60% of the one of the pure tholins for the inter-mixture-L sample (ROI #3) and the intra-mixture-L sample (ROI #1) respectively.

The slowing down observed in the case of the decrease of the reflectance at 0.40 μm and in the case of the increase of the visible red slope, may be due to a decrease of the sublimation rate (and consequently of the building of the mantle) or to a saturation of the tholins absorption at 0.40 μm , the tholins layer becoming optically thick. An analysis of the water band depth data favoured the latter hypothesis (as explained later in this section). Concerning the difference of the final values of the reflectance ($R_{\text{tholins}+10\%}$ vs. $R_{\text{tholins}+50\%}$) and of the red slope (87% vs. 60%), it may be due to a difference of texture of the sublimation deposit, the one from the intra-mixture-L sample being more porous. These data indicate that the long term evolutions of the spectral red slope between 0.40 and 0.94 μm and the reflectance value at 0.40 μm are both affected by the initial mixture type of the ice with the non-volatile organics.

For the inter-mixture-S sample, for which no continuous mantle is formed (see Figure 3), the evolutions of reflectance at 0.40 μm and of the red slope do not follow a smooth curve, as seen in Figure 8a and b. The variations observed are mainly due to movements of aggregates of tholins over the region of interest ROI #5 (see Video 4). For this sample, the reflectance at 0.40 μm decreases and the red slope increases both more than 2 times slower than for the inter-mixture-L and the intra-mixture-L samples.

Water band depth: The Figure 7c and Figure 8c show the evolution of the band depth of the water ice band at 1.51 μm for the different water ice and tholins samples, as well as for the pure water ice sample (ROI #0 on Figure 3). Other water ice absorption bands show similar trends (data not shown). During sublimation, the pure water ice exhibits a slight decrease of the water band depth. This lowering of the band depth may be due to some dust deposit over the sample surface (see Video 1 and section 3.1.1), and/or to a shift of the size distribution of the water ice particles toward the larger particles, slower to sublime. In comparison, the water band depths of the intra-mixture-L samples (as measured over ROI #2, between $t = 2$ and 18h) decrease 14 times faster than that of the pure water ice particles

(Figure 8c). This decrease can be explained by the building of the tholins sublimation mantle over the sample surface, masking the water ice particles located underneath. The water band depths of the inter-mixture-L (ROI #4) and inter-mixture-S samples (ROI #5) also decrease, but possibly at a slower rate than the intra-mixture-L (ROI #2) although the low R^2 values for these linear fits prevent us to give any definitive conclusion (see Figure 8). The data presented in Figure 7c and Figure 8c (near-infrared) appear noisier than the one presented in Figure 7a and Figure 8b (visible), because of a malfunction of the infrared camera as explained in section 2.1. As a consequence, the measured infrared data have been linearly fitted to provide a useful visual guide enabling to compare the trends obtained for the different samples. By comparing the trend of the red slope and the water band depth between 16 and 42 hours for the ROI #1 of the intra-mixture-L sample, it appears that while the red slope remains constant, the water band depth significantly decreases (Figure 7) (this observation can also be made on ROI #2 on Figure 8, between 12 and 18 hours and between 32 and 36 hours). This observation indicates that despite the constant value of the red slope, the tholins mantle continues to increase in thickness deeper in the sample, reducing the depth of the water absorption bands. Therefore the slowing down and plateauing of the red slope is most probably due to a saturation of the tholins absorption band at around $0.40\text{ }\mu\text{m}$, the built tholins layer becoming optically thick at this wavelength. It is also remarkable to notice on Figure 7 and Figure 8 that the water band depth follows a quasi-linear decrease at a constant rate, while the red slope follows a non-linear increase at variable rates.

3.2.2.2 Spectral evolution during ejection of fragments of the tholins mantle

As described in section 3.1, the evolution of the samples during their sublimation is characterized by sudden ejections of fragments of the tholins mantle. Figure 8 shows the spectral evolution of the ROI #2 and ROI #4 where such events occurred at least twice during each simulation (see Videos 3 and 4).

Three ejection events occurred in ROI #2, on the intra-mixture-L sample, at around 20h, 29h and 37h. All are characterized by a sudden:

- surge of reflectance (by +30%, +50% and +160% respectively),
- drop of the red slope (by -15%, -33% and -60% respectively),
- surge of the water band depth (by +30%, +20% and +45% respectively).

These spectral data clearly confirm the ejection of the mantle and the simultaneous exposure of ice particles at the surface of the sample. It must be noted that after the ejection event at 37h, the water band depth of ROI #2 is nearly back to the initial value of the “fresh ice sample” 35h ago (see Figure 8Figure 7c). Following each ejection event, the reflectance at 0.40 μm decreases back toward the pure tholins value while the red slope increases back to the pure tholins value, following exponential-decrease and logarithmic-shaped curves respectively. In the meantime the water band depth linearly decreases as the thickness of the tholins deposit on top of the ice increases. After the ejection events at 29h and 37h, the rates of the water band depth decrease is two times faster than the initial rate observed from $t=2$ to $t=20\text{h}$ (see Figure 8c), probably because of a lower pressure and higher temperature in the simulation chamber, increasing the sublimation rate of the water (see Figure 2).

Two ejection events occurred in ROI #4, on the inter-mixture-L sample, at around 6.5h and 12h. All are characterized by a sudden:

- surge of reflectance (by +150% and +210% respectively),
- drop of the red slope (by -60% and -70% respectively),
- surge of the water band depth (by +10 to +15% for the event at 12h; no data is available for the event at 6.5h).

On average, the surge of reflectance and the drop of the red slope after the ejection events are more intense on the inter-mixture-L sample than on the intra-mixture-L sample. As seen on Videos 3 and 4, after the ejection events, the exposed areas of water ice are still coated by some tholins in the case of the intra-mixture (Video 3) whereas the exposed ice is cleaner in the case of the inter-mixture (Video 4).

Finally, concerning the inter-mixture-S sample, Figure 8Figure 7a and Figure 8Figure 7b show an increase of the reflectance at 0.40 μm and a decrease of the red slope of –about 8 to 20% at 6.5h and 12h. As seen in Video 4, these events are due to the simultaneous ejection of multiple tholins particles initially covering the ice surface.

Mixture type:	intra-mixture		inter-mixture
Ice particles size:	67±31µm	67±31µm	4.5±2.5µm
Sublimation rate:	0.20 mm/h*	0.12 mm/h*	1.06 mm/h
Structure of the sublimation deposit:	foam-like, very porous (>90% porosity) network of filaments extending to the sub-surface (2-5 mm depth), inflated by the gas flow, mantle bound to the ice	skin-like, denser network of filaments, limited to the surface (< 2 mm depth), mantle unstuck/decoupled from the ice	light µm-thin filaments over ice grains, locally formation of dense network of tholins by aggregation, but no surface mantle, residues unstuck/decoupled from the ice
Photometry of mantle formation:	slower decrease of the reflectance at 0.40 µm (exponential), slower increase of the red slope (logarithmic), correlated to a linear decrease of the water band depth	faster decrease of the reflectance at 0.40 µm (exponential), faster increase of the red slope (logarithmic), correlated to a decrease of the water band depth	slower decrease of the reflectance at 0.40 µm (linear), slower increase of the red slope (linear) correlated to a very slow decrease of the water band depth
Activity:	sudden ejection of mantle fragments representing up to more than 50% of the total surface, vibration of the mantle	sudden ejection of mantle fragments representing less than 10% of the total surface, vibration of the mantle	continuous ejection of millimetric size particles, movement of tholins aggregates over the surface
Photometry of mantle ejection:	sudden increase of the reflectance at 0.40 µm from +30 to +160%, sudden decrease of the red slope from -15 to -60%, correlated to an increase of the water band depth from +20 to +45%	sudden increase of the reflectance at 0.40 µm from +150 to +210%, sudden decrease of the red slope from -60 to -70%, correlated to an increase of the water band depth of +10 to +15%	Non Applicable, because continuous activity and ejections of small fragments from the sample surface.
Texture of the ice after simulation:	very thin consolidated crust just below the mantle, underneath texture seems unchanged compared to the initial ice	all the remaining ice below the mantle is consolidated to some extent	texture seems unchanged compared to the initial ice

Table 2: Summary of the results obtained after sublimation experiments n°1 and n°2. *The sublimation rate of pure water ice particles of size 67±31 µm and porosity of 0.5 was about 0.36 mm/h.

4. Discussion

We have studied the sublimation of different mixtures of water ice and tholins. The main results detailed in the previous section are summarized in Table 2. They show how the

initial mixture type and the size of the ice particles influence the properties of the dry deposits obtained after sublimation and the activity of the surface, in term of morphology, texture and spectro-photometric properties.

4.1 Mechanism of mantle building

It appears that when the tholins are present as inclusions within water ice grains, in an intra-mixture, the dry deposit extends both at the surface and at depth as the sublimation occurs. Conversely, when the tholins are coating pure water ice particles (inter-mixture) the dry deposit consists of a thin surficial membrane. Moreover in the case of an inter-mixture, reducing the particle size by a factor of 10 while maintaining the concentration of tholins constant results in the building of very low-cohesiveness filaments at the surface. This is probably due to the spreading out of the tholins over a surface about 100 times larger, impeding the building of a cohesive mantle. The building of filamentary structures from the sublimation of ices containing non-volatiles has been reported by Saunders *et al.* (1986). These authors prepared ice particles made of an intra-mixture of clay and water and analysed the solid residue obtained after sublimation. Ice particles made of an intra-mixture of 0.1% montmorillonite clay in water created a fluffy filamentary residue of $9.10^{-4} \text{ g cm}^{-3}$ density, quite similar to the residue we obtained with the 0.1% intra-mixture sample. Storrs *et al.* (1988) pursued the work of Saunders *et al.* (1986) and noticed that only phyllosilicates and organics were able to form such filamentary sublimate residues (referred to as “FSR”). They explain the formation of these filaments by the electrostatic bonding of charged mineral grains. These grains would become electrically charged during the sublimation of the water molecules that initially surround them or are physically adsorbed on them (see Figure 29 in Sears *et al.*, 1999). The building of filaments and spider web-like structures has also been reported by sublimation of snow-flakes observed under SEM (Rosenthal *et al.*, 2007). These micrometric networks of filaments are made of the non-volatiles contained in the sublimed ice, namely hydrated salts in these cases. These filaments are formed by coalescence of salts, a process by which salt particles merge and change shape to reduce their total surface area, driven by surface diffusion. Sulfur may also have the ability to form filamentous structures (Chevrier *et al.*, 2006). In our case, the non-volatiles consist of a mixture of organic molecules arranged in high porosity spherical grains (coalesced or isolated) having a mean diameter of $315 \pm 185 \text{ nm}$ (Carrasco *et al.*, 2009). As the water sublimates, tholins are moved by the flow of

sublimating gas and can come closer with other particles coming from neighbour ice particles. As they come closer, these nanometric-scale tholins particles can adhere together by intermolecular forces (electrostatic, Van der Waals or hydrogen bonds) and form agglomerates. Hydrogen bonding might be the most efficient interaction sticking the tholins together, as this material is composed of C,H,N-molecules, possessing chemical groups as amines -NH_2 , efficient at forming such H-bonds. The arrangement of these agglomerates of tholins into filamentous networks is probably driven by the reduction of surface energy. Storrs *et al.* (1988) noticed that not all organics have the same abilities to form filamentous residues. Such residues seem to be formed by “volatile rich organics” (tar, water emulsion, tholins used in this study), but not by more refractory organics (kerogen). The loss of “volatiles” (mainly in the form of NH, NH_2 groups in the tholins used in this study) by extensive irradiation (from VUV-UV photons and solar or cosmic energetic particles) may reduce the ability to form hydrogen bonds and such filamentous structure compared to more pristine “volatile rich” organic materials.

Keller and Markiewicz (1991) pointed out that the gravitational field in the laboratory is three orders of magnitude stronger than on a comet and questioned its influence on the results of laboratory simulations. Does gravity play a major role in the building of the mantle in our simulation chamber? Calculations performed by Kochan *et al.* (1990) and Ratke and Kochan (1989) show that some dust particles lying on top of the ice surface are not gravity force dominated. Figure 10 in Ratke and Kochan (1989) shows that the gas drag dominates by two orders of magnitude over gravity for particles (0.3 g/cm^3) smaller than $10 \mu\text{m}$, and that the cohesive forces between particles dominate by several orders of magnitude over gravity (this is especially due to the fact that these experiments were performed at a very low pressure which induces high sublimation rates). In our experiments, the tholin particles, having a mean diameter of around $0.3 \mu\text{m}$, are thus mainly influenced by the gas drag and the cohesive forces. Consequently the impact of gravity seems to be negligible in the building of the sublimation deposit.

Finally, we tentatively observed that the mantle built faster in the case of the inter-mixture compared to the intra-mixture. This may be explained by the fact that when tholins are covering the ice particles (inter-mixture), they are readily put in motion as soon as the sublimation of the particles starts. The tholins can then be moved by the gas flow, approach and stick to other grains to form the filamentous network. Whereas in the case of an intra-mixture, the tholins grains are inside the volume of the ice particles and need to wait longer

before being moved away and available to form the network. Consequently, the mantle building is slower than in the inter-mixture case.

4.2 Mechanism of mantle ejection

While this filamentous mantle is built over the ice surface, the sublimation continues below the mantle and produces a continuous gas flow, or “sublimation wind”, ejecting loosely deposited particles (mm size) or larger fragments (cm size) at different timescales depending on the sample properties. As the mantle increases in thickness, more filaments are built in every direction, and this increases the tortuosity of the path followed by the gas to exit the mantle layer. As the tortuosity increases, the mantle becomes more resistant to the gas flow. The force exerted by the gas on the mantle increases up to the point that it exceeds the tensile strength of the mantle and breaks it in fragments that are ejected away by the gas flow.

In the case of the inter-mixtures we observed a higher rate of ejection and smaller ejected areas than in the case of the intra-mixture (see Table 2). Furthermore, for two mixtures of the same type (inter-mixtures) we have also observed higher rate of ejection and smaller ejected areas in the case of small ice particle sizes compared to larger ice particle sizes. We propose that the efficiency of mantle breaking and ejection depends on how well the mantle is bound to the ice surface. Mantles formed from inter-mixtures appear less efficiently bound to the ice than the one produced from an intra-mixture: unstuck fragments of mantle are seen in Figure 4b and the areas of ice unveiled after the ejection of mantle are still coated by some fragments of tholins in the case of the intra-mixture (Video 3) whereas they appear cleaner in the case of the inter-mixture (Video 4). In the case of a reduced size of the ice particles, the building of the tholins network is less efficient (as described above) and consequently the filamentary residues are even more decoupled from the ice and easy to eject by the gas flow. The differences seen in term of size of the ejected fragments indicate the internal cohesiveness of the mantles, which is stronger in the case of the intra-mixture than in the case of the inter-mixtures.

Moreover, the observation of a solidification of the ice beneath the mantle in the case of the inter-mixture may indicate that the mantle built from an inter-mixture is possibly more resistant to the gas flow than the mantle built from an intra-mixture. This may be due to a denser and more impervious mantle causing a higher pressure inside the ice, increasing the

recondensation of water vapour between the ice particles and consequently solidifying the ice sample. However, while we measured the density and porosity of the “foam-like” sublimation deposit on the intra-mixture-L sample (respectively $5.10^{-4} \text{ g cm}^{-3}$ and $\sim 90\%$), we were unable to do these measurements for the sublimation mantle formed on the inter-mixture-L sample, because of its very thin “skin-like” aspect. Nevertheless, the faster increase of the spectral red slope of the inter-mixture-L compared to the intra-mixture-L (Figure 8b), while the inter-mixture has a lower sublimation rate (Table 2), suggests that the mantle produced from the inter-mixture is probably denser. So we can make the hypothesis that the denser mantle obtained from an inter-mixture is more resistant to the gas flow than the one produced from an intra-mixture which could be more porous and allow water vapour to diffuse through it, preventing a large scale solidification of the ice beneath it. Kochan *et al.* (1989), Ratke and Kochan (1989), Seiferlin *et al.* (1995) and Thiel *et al.* (1989) also observed a solidified crust of ice below an upper mantle.

The observation of outbursts during the sublimation of "dirty ices" has been reported since the 70's by Dobrovolsky and Kajmakow (1977) and references herein. These authors prepared ice from mixtures of minerals and/or organics and observed the formation of a porous matrix and its explosion under sublimation at 10^{-5} - 10^{-6} mbar and 180-240 K. The explosion of the porous matrix ejected fragments at several meters per second. Ejections of mantle fragments were also observed by Thiel *et al.* (1989) and Ratke and Kochan (1989) who proposed that “the fine pores of the coherent mantle impede gas emanation and cause the build-up of gas pressure in the sublimation zone” (...) “the vapor pressure beneath the somewhat more compact dust mantle suddenly increases and breaks up this layer”. This increase of pressure was confirmed by Kömle *et al.* (1991) who measured a pressure build-up of several Pa in covered ice close to the sample surface. Ratke and Kochan (1989) proposed that the erosion of the bonds linking the dust particles to the surface is the main process controlling dust emission. According to Ratke and Kochan (1989) “the particles lift off in that moment when the drag force of the gas jet exceeds the force of gravity and bonding forces” and as we mentioned in section 4.1, they calculated that the bonding force is several orders of magnitude stronger than the gravity force on the particles.

The observation of such ejections of dust particles driven by the sublimation of ice-tholins mixtures can give some clues about the activity of comet nuclei. In particular, the results obtained in the present study show that the sublimation of water ice mixed with

complex organics leads to the emission of mm to cm-sized fluffy aggregates of organics rather than small μm -sized grains.

4.3 Ice-tholins mixtures have lower sublimation rates than pure ice.

The Table 2 indicates that, in our experimental conditions, an intra-mixture of 0.1 wt.% tholins has an average sublimation rate lower by a factor of about 2 compared to pure water ice. An inter-mixture of 0.1 wt.% tholins has an average sublimation rate again a factor of two lower than an intra-mixture. These different sublimation rates are probably due to different regimes of sublimation of the ice depending on the sample: a regime of “free sublimation” for the pure ice (see Equation 21 of Marboeuf *et al.*, 2012), compared to regimes of “diffusion through porous matrix” for the ice sublimating through the more or less dense and tortuous sublimation mantles of inter- and intra- mixture samples (see Equations 28-29 of Marboeuf *et al.*, 2012). One could also speculate that an increase of the pressure in the ice below the sublimation mantle could shift the sublimation temperature to higher values and thus reduce the sublimation rate of the ice particles. The detection of pressure spikes correlated to ejection events, as seen on Figure 2, could be consistent with this hypothesis. Alternatively, this slowing down could also be caused by a reduced thermal conductivity of the porous sublimation mantle compared to the ice (Kömle *et al.*, 1996). To conclude, our experiment clearly shows that a porous sublimation mantle of organics slows down the sublimation of the ice, but without more detailed pressure and temperature data within our samples, the mechanism at the origin of this slowing down is unclear.

4.4 Spectro-photometric properties of the sublimation deposit

Spectroscopically, the building of the sublimation mantle results in the decrease of the reflectance at 0.40 μm and the increase of the visible red slope because of the absorption of the tholins (see Figure 7 and Figure 8a and 8b). This decrease and increase follow exponential and logarithmic-shaped curves respectively, with an asymptote corresponding to the saturation of the tholin absorption band at 0.40 μm . In the case of the inter-mixture sublimation residue, the ~2 mm thick membrane of tholins significantly masks the water absorption bands. This shows that water ice covered with such sublimation lag deposit can easily become invisible to optical and infrared remote sensing. While the reflectance at 0.40

μm follows an exponential decrease and the red slope follows a logarithmic-shaped increase, the water absorption bands follow a linear decrease during the building of the mantle. We tentatively observed that the reflectance at $0.40\ \mu\text{m}$ and the red slope decrease and increase respectively faster for the inter-mixture than for the intra-mixture sample, probably because of different building mechanisms as explained in section 4.1. When the material is too sparse to form a continuous mantle and only loose residues agglomerate and accumulate on the surface or are ejected by the gas flow (as in the case of the inter-mixture-S sample), the reflectance at $0.40\ \mu\text{m}$ and the red slope follow nearly linear decrease and increase respectively (see Figure 8).

The ejections of mantle fragments produce a local increase of the reflectance at $0.40\ \mu\text{m}$ and a decrease of the red slope, correlated to an increase of the water band depth. The intensities of these spectral changes are different for intra-mixtures compared to inter-mixtures. For an inter-mixture the variations of the reflectance at $0.40\ \mu\text{m}$ and the spectral slope are of higher magnitude, while for an intra-mixture the water band depth varies more extensively (see Figure 8c and Table 2). Thus, in the case of the observation a celestial body, a precise monitoring of these spectral changes might provide indications of the way organics are mixed with the ice.

4.5 Application to icy surfaces of celestial bodies

The results of the experiments presented in this paper constitute reference laboratory data that can be used to interpret remote sensing datasets on icy surfaces, including comets, icy satellites or Trans-neptunian Objects for example. One must keep in mind that extrapolations of the details observed on a scale of centimetres in the laboratory to the larger scales observable by planetary or cometary spacecrafts instruments is not obvious and should be done with caution. We describe below some examples of how these laboratory data can be applied to icy surfaces of celestial bodies.

Our measurements of the temporal evolution of the spectral properties of the laboratory samples can serve as a test case to understand the influence of the sublimation process on the spectral properties of the icy surfaces of celestial bodies. For example, the reflectance spectrum of the surface of the comet 67P/Churyumov-Gerasimenko exhibits a red slope from 300 to 1000 nm (Fornasier *et al.*, 2015), most probably due to the presence of a

mantle partly made of complex organic matter covering the ice (Capaccioni *et al.*, 2015). Our laboratory data on ice-tholins analogue mixtures suggest that variations of the surface reflectance and steepness of the red slope observed on the cometary surface may be indicative of the thickness of the organic mantle covering ice material. For instance, based on our observations made in the laboratory, Pommerol *et al.* (2015b) hypothesized that the bright spots seen at the surface of 67P/Churyumov-Gerasimenko by the OSIRIS camera onboard Rosetta are “areas where the dust mantle has not reformed or has not reached yet a sufficient thickness to hide the icy material below”. By plotting the spectral ratios between the reflectance spectra obtained before and after the formation of the sublimation mantle and comparing these ratios to those observed on the comet, Pommerol *et al.* (2015b) showed that the contrasts of brightness and colour seen at the surface of the nucleus were consistent with the result of sublimation process (see Fig. 9 and Fig. 11 in Pommerol *et al.*, 2015b). A similar method could be applied to compare the data obtained from the surface of Pluto by the instruments on-board New Horizon with our laboratory data. Indeed, the surface of Pluto contains ices most likely mixed with complex organic matter exhibiting a visible red slope and subjected to sublimation processes (Cruikshank *et al.*, 2015). Additionally, the documentation of the evolution of the reflectance of the continuum and the water band depth in the near infrared can also support the interpretation of the data gathered by infrared spectrometers on-board Rosetta or New Horizon spacecrafts for example. For such comparison and interpretation purposes (calculation of spectral ratios, calculation of spectral slopes or band depths with other wavelengths or definitions, etc.), the calibrated hyperspectral data of all the ROIs presented in this paper on Figures 6, 7 and 8 are available upon demand to the corresponding author.

Furthermore, the evolution of the structure and physical properties of the analogue samples during sublimation also provides interesting clues to understand the surface of cometary nucleus, TNOs or icy satellites. Ice-tholins samples placed under simulated comet surface conditions acquire a vertical stratification with an uppermost porous mantle of refractory tholins overlaying a layer of hard ice formed by re-condensation/sintering under the mantle. The ability of tholins particles to build bounds between them can help to explain the formation and ejection of large dust grains in jets and their deposition as “airfall” on cometary nuclei (Thomas *et al.*, 2015). The hardening of the ice below the sublimation mantle, as observed in laboratory experiments, also provides a plausible mechanism to explain the observation of brittle mechanical behaviour of some regions on the surface of

67P/Churyumov-Gerasimenko (Pommerol *et al.*, 2015b). Moreover, we observed that the cohesiveness of the mantle and the hardening of the ice layer strongly depend on the way the non-volatile components are initially mixed with the ice. As we mentioned in the introduction, the way the ice and the non-volatiles are mixed at the surface of the comet is poorly known. Differences seen in term of mantle structure, sublimation speed, speed of mantle building, rates and surface area of mantle ejection, between intra- and inter- mixtures might provide clues to discriminate between these mixture types on cometary nuclei surfaces or on other surfaces of air-less bodies where dirty ices are sublimating. Finally, the development of such vertical stratification and change of textures upon sublimation are also important for the evolution of the surface thermal properties observed on comets and other icy bodies, although this point was not the focus of the analysis of the experiments presented in this paper.

Conclusion

We have presented in this article the sublimation of samples of water ice mixed with tholins, analogs of complex organic matter found in extraterrestrial environments. Samples prepared using different mixture types and different water ice particle sizes, but all containing the same mass ratio of tholins, have been sublimed, and their evolutions have been compared. The results are summarized in Table 2 and in the points below:

- **All ice-tholins mixtures produce an ice-free residue of tholins during sublimation:** in the form of a mantle covering the ice in the case of ice particles of $67\pm 31\ \mu\text{m}$ or in the form of aggregates in the case of ice particles of $4.5\pm 2.5\ \mu\text{m}$, for a tholins/water mass ratio of 0.1%.
- The **mixing mode** of the water ice with the tholins, as well as the **ice particle size**, both strongly influence the evolution of the samples during sublimation, their the sublimation rate, as well as the structure and the activity of the sublimation lag deposit.
- **The mantle produced from an intra-mixture has a higher porosity (>90%), a stronger cohesiveness, and is more efficiently bound to the ice particles than the mantle produced from an inter-mixture.** The first one resembles a 2 to 5 mm thick foam while the second one resembles a skin less than 2 mm thick.

- **Sudden ejections of large fragments of these mantles, from mm to cm sizes, are observed during the sublimation**, probably triggered by sudden increases of pressure in the ice below the mantles. More cohesive mantles produce larger fragments. Continuous vibrations of the mantles, or movements of the aggregates are observed at the surface of the samples.
- As the tholins mantles are built over the sample surfaces, the reflectance at 0.40 μm (where tholins absorb light) decreases, with an exponential-like trend, while inversely the visible red slope (from 0.40 to 0.94 μm) increases, with a logarithmic-like trend, up to the values of the pure tholins powder. These variations are faster in the case of the inter-mixture than in the case of an intra-mixture. In the meantime, the depth of the water absorption bands decreases linearly. **The smallest water absorption bands are almost completely masked by a porous layer of tholins less than 5 mm thick.**
- Interestingly, we observed that while the depth of the water absorption bands in the infrared continues to decrease, the tholins spectral features (reflectance at 0.40 μm and red slope) remain constant in the visible. This indicates that **the tholins layer rapidly becomes optically thick in the visible**, stopping any further spectral evolution in this wavelength range while continuing to increase in thickness deeper in the sample.
- **The ejections of large fragments of mantles expose bright ice particles to the surface of the samples.** These events result in the sudden increase of the reflectance at 0.40 μm by +30 to +210%, the sudden decrease of the visible red slope by -15 to -70%, correlated to an increase of the water bands depth by +10 to +45%. In the case of an inter-mixture, these variations are of higher magnitude compared to an intra-mixture because of the exposure of cleaner ice due to the lower cohesiveness between the mantle and the ice.
- **The mixing mode of the ice with the tholins appears to play a role in the sintering of the ice particles below the mantle.** The ice of an inter-mixture sample sinters much more efficiently than the ice of an intra-mixture. The mantle of tholins produced from an inter-mixture favours the recondensation of the water vapour between the ice particles.

These data provide useful references for interpreting remote sensing observations of icy Solar System surfaces. In particular, they can provide some elements of explanation regarding the activity of comet nuclei where sublimation of organic-rich ices and deposition of organic-dust particles play a major role.

Although this experiment is, to our knowledge, the first performed with a mixture of water ice and tholins at such concentrations, the amount of tholins incorporated into the mixture is still small in comparison to what we could expect in a comet for example. Estimates of dust/ice ratio for comets go from 0.5 to 2 or more (Kuppers *et al.*, 2005; Marboeuf *et al.*, 2014; Weiler *et al.*, 2004) and estimates of organics/minerals ratio go from 0.3 to 1 (Fomenkova, 1999; Huebner, 2003; Jessberger *et al.*, 1989). By comparison, all the samples we have prepared for the present study have an organics/ice ratio of 0.001. The effect of higher concentrations of organics will have to be assessed in future experiments. Furthermore, the influence of minerals (olivine, phyllosilicates etc.) will also have to be characterized. As we discussed in section 4, previous sublimation experiments made on mixtures of minerals and water ice provide similar results in term of mantle morphology and activity. But did minerals behave the same as tholins when specifically mixed in intra- or inter- mixture? And how are their reflectance features influenced by the mantle morphology?

From the irradiation point of view, we are also planning to illuminate the samples with a Sun simulator that will provide a more realistic spectral irradiance. Indeed, the sublimation observed in this study has been triggered by infrared radiations coming from the upper window of the simulation chamber, so it will be important to test the impact of visible light on the results.

Finally, the porous mantle obtained after sublimation has certainly an important effect on the scattering of the light. Future measurement of the bidirectional reflectance of such evolved samples, obtained in SCITEAS, using the PHIRE-2 radiogoniometer also developed in the LOSSy (Pommerol *et al.*, 2011) will certainly provide new clues to improve our understanding of past, current and future optical remote-sensing datasets acquired on icy Solar System surfaces.

Acknowledgements

The construction of the SCITEAS facility was funded by the University of Bern and by the Swiss National Science Foundation. O.P. thanks the Center for Space and Habitability of the University of Bern for funding. We thank Sonia Fornasier and Ulysse Marboeuf for useful discussions relative to this manuscript. The authors acknowledge the reviews of

Vincent Chevrier and an anonymous reviewer for their comments and suggestions which significantly improved the manuscript.

Supplementary Material

Videos can be found on <http://dx.doi.org/10.1016/j.icarus.2015.11.006> or can be obtained directly from the author by email (olivier.poch@csh.unibe.ch).

The text below provides a detailed description and analysis of the videos depicting the evolution of the samples during the 45 hours of the experiment n°1 (Video 1) and the 13 hours of experiment n°2 (Video 2). To facilitate the interpretation of the videos by the reader, the time values given in the text below referred to the time shown on each frame of Videos 1 and 2.

Experiment n°1 (Video 1): tholins intra-mixture-L and pure “L”-water ice samples

From 0 to 19.02h: The frost covering the sample holder sublimates from 0 to 14.04 h. Very fine particles are ejected from the pure water ice sample, some stick to the quartz window and cast shadow on the samples as can be seen between 13.43-13.45 h, 13.45-13.47 h, 13.64-14.02 h, 14.98-15.35 h etc. These residues probably come from contaminants in the distilled water used to prepare the ice particles (salts, dust etc.). Microscopic images (data not shown) indicate that these residues are made of very fine, sub-micrometric "dust" particles. In the meantime, no particle is emitted from the tholins intra-mixture-L sample. The morphology of its surface changes from an initial slightly rough ice surface with some colour inhomogeneities to a more colour-uniform, darker and smoother surface. As the water ice sublimates, a deposit made of the non-volatiles compounds initially present in the ice builds up at the surface of the ice samples, causing these changes of colour and texture. This deposit is designated as the “sublimation mantle” or the “sublimation lag deposit” in the following paragraphs.

From 19.02 to 44.69 h: Between 19.02 and 19.04 h, a sudden release of material from nearly half the surface of the top sublimated layer of the tholins intra-mixture-L sample occurs and spreads fragments of the layer over the sample holder. The area from where the material was released appears brighter on the visible images. This bright material is made of the mixture of

water ice and tholins, initially located below the sublimation mantle, which is now exposed to the top of the sample, as confirmed by its near infrared spectrum (see ROI #2, Figure 7). Simultaneously, the pressure in the chamber suddenly increases by $+3.10^{-6}$ mbar. Afterwards, the pressure slowly goes back (in about 2.7 hours) to its initial value before the mantle release. In the meantime, the bright area of exposed fresh ice becomes darker as the ice sublimates, rebuilding the tholins mantle. From 19.04 to 27.70 h, the Video 1 also shows the constant shaking of some fragments of the initial sublimation layer still attached to the sample surface. This shaking is probably due to the flow of water vapour coming from the sublimation of the ice below the dust mantle.

Other episodes of sudden release of the dust mantle are observed between 27.70-27.72 h, 29.74-30.12 h, 32.35-32.72 h, 35.60-35.98 h, 42.13-42.51 h and 43.77-43.89 h. Some of these episodes release more than 50% of the surface of the mantle (between 27.70-27.72 h and 35.60-35.98 h) while the others are confined to smaller areas. Some of these episodes are correlated to an increase of pressure (see the red dashed lines in Figure 2). Fragments are ejected all over the sample holder and deposit on the pure water ice sample, on the calibration target, as well as on the window of the chamber where they remained stuck.

After about 29 h, the dark bottom of the sample holder becomes visible at the centre of the pure water ice sample while there is still a large amount of water ice in the tholins intra-mixture-L sample. Comparison of pre- and post- simulation sample thickness indicates that the sublimation of the pure water ice sample was nearly a factor of 2 faster than the sublimation of the tholins intra-mixture-L sample (see Table 2 for the values of sublimation rates measured for all samples).

In the pure water ice sample, several circular depressions are developed and expand in diameter as the sublimation of the ice goes on. Similar circular depressions were seen during the comet #1 experiment (Pommerol *et al.*, 2015a). The fact that both of these samples were deposited with liquid nitrogen and that no such features are observed in samples deposited by sieving (see Figure 3 and Video 2) indicates that these circular features originate from voids formed inside the sample during the evaporation of liquid nitrogen.

From 44.00 h to the end: At 43.5 h, the circulation of liquid nitrogen in the shroud is stopped. As the nitrogen evaporates, the temperature of the shroud increases and the water frost covering the shroud sublimates, increasing the pressure in the chamber. The Video 1 shows that some parts of the tholins mantle are still vibrating up to a pressure of the order of 0.01

mbar. This indicates that the sublimation of the water below the mantle is still strong enough to move the mantle. When the pressure reaches more than about 0.1 mbar, the vibrations stop and a subsidence movement of the whole mantle can be seen between 44.69 and 45.22 h. This subsidence indicates that the flow of water vapour was responsible for the inflation of the whole mantle (a high resolution image of the inflated mantle can be seen in Figure 4a).

Experiment n°2 (Video 2): tholins inter-mixture-L and inter-mixture-S samples

From 0 to 1.5 h: Both samples get darker. The inter-mixture-L sample gets a homogeneous darker colour while the inter-mixture-S sample gets speckled, covered by numerous dark dots smaller than 1mm. Between 0.86 and 1.36 h, the sample holder moved which is probably the cause of the formation of the cracks in the ice observed after 1.36 h on the large size particles sample.

From 1.5 to 3.3 h: During this period, while the inter-mixture-L sample gets simply darker, the inter-mixture-S sample undergoes a very dynamic evolution. The small dark dots covering its surface are concentrically ejected from the left centre of the sample. This geometric evolution is possibly due to the heterogeneity of the temperature inside the ice sample because of the shape of the sample holder, the centre being warmer than the sides. (The temperature at the centre and the sides was not measured, but this hypothesis is based on the observation that the rate of sublimation is lower close to the border of the sample holder than at the centre, as seen on Video 1 and Video 2. This effect applies to all the samples.) Two such “waves” of concentric ejections can be spotted: the first one starting around 1.5 h and the second one after 2.61 h. The tholins ejected during these events hit the upper window, casting shadow in the form of small dots on the sample holder and on the other sample. One should also note that as a consequence of this concentric “wave” some tholins accumulate all around the rim of the sample.

From 3.30 to 5.71 h: No more concentric ejections are observed for the inter-mixture-S sample. Ejections continue at the same rate, but from random locations at the surface of the sample. The surface texture is no more organized in small dots, but in more uneven dark spots that become darker, probably by aggregation of tholins, before being ejected by the gas flow.

At around 4.9 h the temperature sensor starts to be excavated from the inter-mixture-S sample, and a cavity is formed by the sublimation of the ice and starts to expand around it.

From 5.71 h to 10.22 h: Between 5.71 and 6.06 h, a fragment of tholins mantle is ejected from the inter-mixture-L sample, exposing bright fresh water ice particles to the surface. Afterwards, the exposed ice progressively darkens as the mantle is re-built. This ejection event is responsible for the pressure spike seen at 5.80 h in Figure 2b. The pressure increases by $+3.10^{-6}$ mbar and comes back to its previous value before the ejection in less than 7 minutes.

Several other ejections occurred between 6.40-6.76 h, 7.00-7.02 h, 8.16-8.18 h, 8.48-8.83 h, 9.17-9.52 h, 9.60-9.62 h etc. The 6.40-6.76 h event could be correlated to a pressure spike seen at 6.43 h in Figure 2b. At 7.1h the circulation of liquid nitrogen in the shroud is reduced, resulting in an increase of the pressure in the chamber, and the other ejection events cannot be correlated to a specific pressure spike. All these events are characterized by the ejection of irregular-shaped areas always representing less than 10% of the total surface of the sample (see Figure 3). The mantle fragments ejected by the inter-mixture-L sample are similar to a skin just 1 or 2 mm thick, which looks more compact than the very fluffy mantle obtained by sublimation of the intra-mixture-L sample (see Figure 3 and Figure 4a,b).

In the meantime, the evolution of the inter-mixture-S sample is characterized by the migration of the tholins accumulated around the rim toward the centre of the sample. While migrating, these aggregates of tholins grow in size. This migration backward is due to dragging by the gas flow coming from the ice located at the border of the sample holder. The initially flat sample surface gets excavated in a bowl-shape as the ice sublimates, the sublimation rate being slower at the border of the sample holder.

From 10.22 h to 13.29 h: At around 9 h, the circulation of liquid nitrogen in the shroud is stopped, leading to an increase of temperature and pressure in the chamber. An acceleration of the sublimation rate for both samples is observed. Between 11.15 and 12.50 h, on the inter-mixture-S sample, a very fine mantle of small dark dots is built and is progressively ejected, while on the inter-mixture-L sample a total of 10 ejections of mantle areas occurs.

From 13.29 h to the end: As the pressure in the chamber increases from 0.1 to 471 mbar, a noticeable compression of the tholins layers or aggregates present on the sample surfaces occurs.

References:

Altwegg, K., Balsiger, H., Bar-Nun, A., Berthelier, J.J., Bieler, A., Bochslers, P., Briois, C., Calmonte, U., Combi, M., De Keyser, J., Eberhardt, P., Fiethe, B., Fuselier, S., Gasc, S., Gombosi, T.I., Hansen, K.C., Hässig, M., Jäckel, A., Kopp, E., Korth, A., LeRoy, L., Mall, U., Marty, B., Mousis, O., Neefs, E., Owen, T., Rème, H., Rubin, M., Sémon, T., Tzou, C.-Y., Waite, H., Wurz, P., **2015**. 67P/Churyumov-Gerasimenko, a Jupiter family comet with a high D/H ratio. *Science* 347.

Andronico, G., Baratta, G., Spinella, F., Strazzulla, G., **1987**. Optical evolution of laboratory-produced organics-Applications to Phoebe, Iapetus, outer belt asteroids and cometary nuclei. *Astronomy and Astrophysics* 184, 333-336.

Belton, M.J.S., Thomas, P., Veverka, J., Schultz, P., A'Hearn, M.F., Feaga, L., Farnham, T., Groussin, O., Li, J.Y., Lisse, C., McFadden, L., Sunshine, J., Meech, K.J., Delamere, W.A., Kissel, J., **2007**. The internal structure of Jupiter family cometary nuclei from Deep Impact observations: The "talps" or "layered pile" model. *Icarus* 187, 332-344.

Bennett, C.J., Pirim, C., Orlando, T.M., **2013**. Space-Weathering of Solar System Bodies: A Laboratory Perspective. *Chem. Rev.* 113, 9086-9150.

Berger, R., **1961**. The proton irradiation of methane, ammonia, and water at 77 K. *Proc. Natl. Acad. Sci. U. S. A.* 47, 1434.

Bernard, J.-M., Quirico, E., Brissaud, O., Montagnac, G., Reynard, B., McMillan, P., Coll, P., Nguyen, M.-J., Raulin, F., Schmitt, B., **2006**. Reflectance spectra and chemical structure of Titan's tholins: Application to the analysis of Cassini-Huygens observations. *Icarus* 185, 301-307.

Bonnet, J.-Y., Quirico, E., Buch, A., Thissen, R., Szopa, C., Carrasco, N., Cernogora, G., Fray, N., Cottin, H., Roy, L.L., Montagnac, G., Dartois, E., Brunetto, R., Engrand, C., Duprat, J., **2015**. Formation of analogs of cometary nitrogen-rich refractory organics from thermal degradation of tholin and HCN polymer. *Icarus* 250, 53-63.

Byrne, S., **2009**. The Polar Deposits of Mars. *Annual Review of Earth and Planetary Sciences* 37, 535-560.

Byrne, S., Dundas, C.M., Kennedy, M.R., Mellon, M.T., McEwen, A.S., Cull, S.C., Daubar, I.J., Shean, D.E., Seelos, K.D., Murchie, S.L., Cantor, B.A., Arvidson, R.E., Edgett, K.S., Reufer, A., Thomas, N., Harrison, T.N., Posiolova, L.V., Seelos, F.P., **2009**. Distribution of Mid-Latitude Ground Ice on Mars from New Impact Craters. *Science* 325, 1674-1676.

Capaccioni, F., Coradini, A., Filacchione, G., Erard, S., Arnold, G., Drossart, P., De Sanctis, M.C., Bockelee-Morvan, D., Capria, M.T., Tosi, F., Leyrat, C., Schmitt, B., Quirico, E., Cerroni, P., Mennella, V., Raponi, A., Ciarniello, M., McCord, T., Moroz, L., Palomba, E., Ammannito, E., Barucci, M.A., Bellucci, G., Benkhoff, J., Bibring, J.P., Blanco, A., Blecka, M., Carlson, R., Carsenty, U., Colangeli, L., Combes, M., Combi, M., Crovisier, J., Encrenaz, T., Federico, C., Fink, U., Fonti, S., Ip, W.H., Irwin, P., Jaumann, R., Kuehrt, E., Langevin, Y., Magni, G., Mottola, S., Orofino, V., Palumbo, P., Piccioni, G., Schade, U., Taylor, F., Tiphene, D., Tozzi, G.P., Beck, P., Biver, N., Bonal, L., Combe, J.-P., Despan, D., Flamini, E., Fornasier, S., Frigeri, A., Grassi, D., Gudipati, M., Longobardo, A., Markus, K., Merlin, F., Orosei, R., Rinaldi, G., Stephan, K., Cartacci, M., Cicchetti, A., Giuppi, S., Hello, Y., Henry, F., Jacquino, S., Noschese, R., Peter, G., Politi, R., Reess, J.M., Semery, A., **2015**. The organic-rich surface of comet 67P/Churyumov-Gerasimenko as seen by VIRTIS/Rosetta. *Science* 347.

Carrasco, N., Schmitz-Afonso, I., Bonnet, J.Y., Quirico, E., Thissen, R., Dutuit, O., Bagag, A., Laprévote, O., Buch, A., Giuliani, A., Adandé, G., Ouni, F., Hadamcik, E., Szopa, C., Cernogora, G., **2009**. Chemical Characterization of Titan's Tholins: Solubility, Morphology and Molecular Structure Revisited†. *The Journal of Physical Chemistry A* 113, 11195-11203.

Chevrier, V., Mathé, P.-E., Rochette, P., Grauby, O., Bourrié, G., Trolard, F., **2006**. Iron weathering products in a CO₂ + (H₂O or H₂O₂) atmosphere: Implications for weathering processes on the surface of Mars. *Geochimica et Cosmochimica Acta* 70, 4295-4317.

Clark, R. N., Cruikshank, D. P., Jaumann, R., Brown, R. H., Stephan, K., Dalle Ore, C. M., Livio, K. E., Pearson, N., Curchin, J. M., Hoefen, T. M., Buratti, B. J., Filacchione, G., Baines, K. H., and Nicholson, P. D., **2012**. The surface composition of Iapetus: Mapping results from Cassini VIMS. *Icarus* 218, 831-860.

Colaprete, A., Schultz, P., Heldmann, J., Wooden, D., Shirley, M., Ennico, K., Hermalyn, B., Marshall, W., Ricco, A., Elphic, R.C., Goldstein, D., Summy, D., Bart, G.D., Asphaug, E., Korycansky, D., Landis, D., Sollitt, L., **2010**. Detection of Water in the LCROSS Ejecta Plume. *Science* 330, 463-468.

Cruikshank, D., **2005**. Triton, Pluto, Centaurs, and Trans-Neptunian Bodies, In: Encrenaz, T., Kallenbach, R., Owen, T.C., Sotin, C. (Eds.), *The Outer Planets and their Moons*. Springer Netherlands, pp. 421-439.

Cruikshank, D.P., Grundy, W.M., DeMeo, F.E., Buie, M.W., Binzel, R.P., Jennings, D.E., Olkin, C.B., Parker, J.W., Reuter, D.C., Spencer, J.R., Stern, S.A., Young, L.A., Weaver, H.A., **2015**. The surface compositions of Pluto and Charon. *Icarus* 246, 82-92.

Cruikshank, D.P., Imanaka, H., Dalle Ore, C.M., **2005**. Tholins as coloring agents on outer Solar System bodies. *Advances in Space Research* 36, 178-183.

de Bergh, C., Schmitt, B., Moroz, L.V., Quirico, E., Cruikshank, D.P., **2008**. Laboratory Data on Ices, Refractory Carbonaceous Materials, and Minerals Relevant to Transneptunian Objects and Centaurs, In: Barucci, A. (Ed.), *The Solar System Beyond Neptune*. University of Arizona Press.

Derenne, S., Robert, F., Skrzypczak-Bonduelle, A., Gourier, D., Binet, L., Rouzaud, J.-N., **2008**. Molecular evidence for life in the 3.5 billion year old Warrawoona chert. *Earth and Planetary Science Letters* 272, 476-480.

Dobrovolsky, O., Kajmakow, E., **1977**. Surface phenomena in simulated comet nuclei, In: Delsemme, A.H. (Ed.), *Comets, Asteroids, Meteorites*, pp. 37-46.

Duffard, R., Pinilla-Alonso, N., Santos-Sanz, P., Vilenius, E., Ortiz, J.L., Mueller, T., Fornasier, S., Lellouch, E., Mommert, M., Pal, A., Kiss, C., Mueller, M., Stansberry, J., Delsanti, A., Peixinho, N., Trilling, D., **2014**. “TNOs are Cool”: A survey of the trans-Neptunian region. *A&A* 564, A92.

Fomenkova, M.N., **1999**. On the Organic Refractory Component of Cometary Dust. *Space Science Reviews* 90, 109-114.

Fornasier, S., Hasselmann, P. H., Barucci, M.A., Feller, C., Besse, S., Leyrat, C., L. Lara, P. J. Gutierrez, N. Oklay, C. Tubiana, F. Scholten, H. Sierks, C. Barbieri, P. L. Lamy, R. Rodrigo, D. Koschny, H. Rickman, H. U. Keller, J. Agarwal, M. F. A'Hearn, J.-L. Bertaux, I. Bertini, G. Cremonese, V. Da Deppo, B. Davidsson, S. Debei, M. De Cecco, M. Fulle, O. Groussin, C. Güttler, S. F. Hviid, W. Ip, L. Jorda, J. Knollenberg, G. Kovacs, R. Kramm, E. Kürt, M. Küppers, F. La Forgia, M. Lazzarin, J. J. Lopez Moreno, F. Marzari, K.-D. Matz, H. Michalik, F. Moreno, S. Mottola, G. Naletto, M. Pajola, A. Pommerol, F. Preusker, X. Shi, C. Snodgrass, N. Thomas, J.-B. Vincent, **2015**. Spectrophotometric properties of the nucleus of comet 67P/Churyumov-Gerasimenko from the OSIRIS instrument onboard the ROSETTA spacecraft. *Astronomy and Astrophysics*, in press.

Fulchignoni, M., Ferri, F., Angrilli, F., Ball, A.J., Bar-Nun, A., Barucci, M.A., Bettanini, C., Bianchini, G., Borucki, W., Colombatti, G., Coradini, M., Coustenis, A., Debei, S., Falkner, P., Fanti, G., Flamini, E., Gaborit, V., Grard, R., Hamelin, M., Harri, A.M., Hathi, B., Jernej, I., Leese, M.R., Lehto, A., Lion Stoppato, P.F., Lopez-Moreno, J.J., Makinen, T., McDonnell, J.A.M., McKay, C.P., Molina-Cuberos, G., Neubauer, F.M., Pirronello, V., Rodrigo, R., Saggin, B., Schwingenschuh, K., Seiff, A., Simoes, F., Svedhem, H., Tokano, T., Towner, M.C., Trautner, R., Withers, P., Zarnecki, J.C., **2005**. In situ measurements of the physical characteristics of Titan's environment. *Nature* 438, 785-791.

Gautier, T., Carrasco, N., Buch, A., Szopa, C., Sciamma-O'Brien, E., Cernogora, G., **2011**. Nitrile gas chemistry in Titan's atmosphere. *Icarus* 213, 625-635.

Geissler, P.E., McEwen, A.S., Keszthelyi, L., Lopes-Gautier, R., Granahan, J., Simonelli, D.P., **1999**. Global Color Variations on Io. *Icarus* 140, 265-282.

Gombosi, T.I., Houppis, H.L.F., **1986**. An icy-glue model of cometary nuclei. *Nature* 324, 43-44.

Greenberg, J.M., **1998**. Making a comet nucleus. *Astronomy and Astrophysics* 330, 375-380.

Greenberg, J.M., Li, A., **1999**. Morphological structure and chemical composition of cometary nuclei and dust. *Space Science Reviews* 90, 149-161.

Grün, E., Kochan, H., Seidensticker, K.J., **1991**. Laboratory simulation, A tool for comet research. *Geophysical Research Letters* 18, 245-248.

Hadamcik, E., Renard, J., Mahjoub, A., Gautier, T., Carrasco, N., Cernogora, G., Szopa, C., **2013**. Optical properties of analogs of Titan's aerosols produced by dusty plasma. *Earth Planets Space* 65, 1175-1184.

Hartmann, W.K., Tholen, D.J., Cruikshank, D.P., **1987**. The relationship of active comets, "extinct" comets, and dark asteroids. *Icarus* 69, 33-50.

Herbst, E., Van Dishoeck, E.F., **2009**. Complex organic interstellar molecules. *Annual Review of Astronomy and Astrophysics* 47, 427-480.

Huebner, W., **2003**. Composition of Comets: Observations and Models, In: Boehnhardt, H., Combi, M., Kidger, M.R., Schulz, R. (Eds.), *Cometary Science after Hale-Bopp*. Springer Netherlands, pp. 179-195.

Imanaka, H., Khare, B.N., Elsila, J.E., Bakes, E.L.O., McKay, C.P., Cruikshank, D.P., Sugita, S., Matsui, T., Zare, R.N., **2004**. Laboratory experiments of Titan tholin formed in cold plasma at various pressures: implications for nitrogen-containing polycyclic aromatic compounds in Titan haze. *Icarus* 168, 344-366.

Jessberger, E.K., Kissel, J., Rahe, J., **1989**. The composition of comets, Origin and evolution of planetary and satellite atmospheres, pp. 167-191.

Johnson, R.E., Cooper, J.F., Lanzerotti, L.J., Strazzulla, G., **1988**. Radiation formation of a non-volatile comet crust, In: Grewing, M., Praderie, F., Reinhard, R. (Eds.), *Exploration of Halley's Comet*. Springer Berlin Heidelberg, pp. 889-892.

Jost, B., Pommerol, A., Poch, O., Gundlach, B., Leboeuf, M., Dardas, M., Blum, J., Thomas, N., Experimental characterization of the opposition surge in fine-grained water-ice and high albedo analogs, under review in *Icarus*

Keller, H.U., Markiewicz, W.J., **1991**. KOSI? *Geophysical Research Letters* 18, 249-252.

Kochan, H., Ratke, L., Thiel, K., Grun, E., **1990**. Particle emission from artificial cometary surfaces-Material science aspects, Lunar and Planetary Science Conference Proceedings, pp. 401-411.

Kochan, H., Roessler, K., Ratke, L., Heyl, M., Hellmann, H., Schwehm, G., **1989**. Crustal strength of different model comet materials, Physics and Mechanics of Cometary Materials, pp. 115-119.

Kömle, N.I., Kargl, G., Thiel, K., Seiferlin, K., **1996**. Thermal properties of cometary ices and sublimation residua including organics. *Planetary and Space Science* 44, 675-689.

Kömle, N.I., Steiner, G., Dankert, C., Dettleff, G., Hellmann, H., Kochan, H., Baguhl, M., Kohl, H., Kölzer, G., Thiel, K., Öhler, A., **1991**. Ice sublimation below artificial crusts: Results from comet simulation experiments. *Planetary and Space Science* 39, 515-524.

Kuppers, M., Bertini, I., Fornasier, S., Gutierrez, P.J., Hviid, S.F., Jorda, L., Keller, H.U., Knollenberg, J., Koschny, D., Kramm, R., Lara, L.-M., Sierks, H., Thomas, N., Barbieri, C., Lamy, P., Rickman, H., Rodrigo, R., The, O.t., **2005**. A large dust/ice ratio in the nucleus of comet 9P/Tempel 1. *Nature* 437, 987-990.

Mahjoub, A., Carrasco, N., Dahoo, P.-R., Gautier, T., Szopa, C., Cernogora, G., **2012**. Influence of methane concentration on the optical indices of Titan's aerosols analogues. *Icarus*.

Marboeuf, U., Schmitt, B., Petit, J.-M., Mousis, O., Fray, N., **2012**. A cometary nucleus model taking into account all phase changes of water ice: amorphous, crystalline, and clathrate★. *Astronomy & Astrophysics* 542, A82.

Marboeuf, U., Thiabaud, A., Alibert, Y., Cabral, N., Benz, W., **2014**. From planetesimals to planets: volatile molecules. *Astronomy & Astrophysics* 570, A36.

McDonald, G.D., Thompson, W.R., Heinrich, M., Khare, B.N., Sagan, C., **1994**. Chemical Investigation of Titan and Triton Tholins. *Icarus* 108, 137-145.

Meador, M.A.B., Malow, E.J., Silva, R., Wright, S., Quade, D., Vivod, S.L., Guo, H., Guo, J., Cakmak, M., **2012**. Mechanically Strong, Flexible Polyimide Aerogels Cross-Linked with Aromatic Triamine. *ACS Appl. Mater. Interfaces* 4, 536-544.

Moore, J.M., Black, G., Buratti, B., Phillips, C.B., Spencer, J., Sullivan, R., **2009**. Surface properties, regolith, and landscape degradation, Europa, pp. 329-349.

Moroz, L., Baratta, G., Strazzulla, G., Starukhina, L., Dotto, E., Barucci, M.A., Arnold, G., Distefano, E., **2004**. Optical alteration of complex organics induced by ion irradiation:: 1. Laboratory experiments suggest unusual space weathering trend. *Icarus* 170, 214-228.

Neish, C.D., Barnes, J.W., Sotin, C., MacKenzie, S., Soderblom, J.M., Le Mouélic, S., Kirk, R.L., Stiles, B.W., Malaska, M.J., Le Gall, A., Brown, R.H., Baines, K.H., Buratti, B., Clark, R.N., Nicholson, P.D., **2015**. Spectral properties of Titan's impact craters imply chemical weathering of its surface. *Geophysical Research Letters* 42, 3746-3754.

Neumann, G.A., Cavanaugh, J.F., Sun, X., Mazarico, E.M., Smith, D.E., Zuber, M.T., Mao, D., Paige, D.A., Solomon, S.C., Ernst, C.M., Barnouin, O.S., **2013**. Bright and Dark Polar Deposits on Mercury: Evidence for Surface Volatiles. *Science* 339, 296-300.

Oehler, A., Neukum, G., **1991**. Visible and near IR albedo measurements of ice/dust mixtures. *Geophysical Research Letters* 18, 253-256.

Ozgür Engin, N., Tas, A.C., **1999**. Manufacture of macroporous calcium hydroxyapatite bioceramics. *Journal of the European Ceramic Society* 19, 2569-2572.

Paige, D.A., Siegler, M.A., Harmon, J.K., Neumann, G.A., Mazarico, E.M., Smith, D.E., Zuber, M.T., Harju, E., Delitsky, M.L., Solomon, S.C., **2013**. Thermal Stability of Volatiles in the North Polar Region of Mercury. *Science* 339, 300-303.

Pernot, P., Carrasco, N., Thissen, R., Schmitz-Afonso, I., **2010**. Tholinomics—Chemical analysis of nitrogen-rich polymers. *Anal. Chem.* 82, 1371-1380.

Pieters, C.M., Goswami, J.N., Clark, R.N., Annadurai, M., Boardman, J., Buratti, B., Combe, J.-P., Dyar, M.D., Green, R., Head, J.W., Hibbitts, C., Hicks, M., Isaacson, P., Klima, R., Kramer, G., Kumar, S., Livo, E., Lundeen, S., Malaret, E., McCord, T., Mustard, J., Nettles, J., Petro, N., Runyon, C., Staid, M., Sunshine, J., Taylor, L.A., Tompkins, S., Varanasi, P., **2009**. Character and Spatial Distribution of OH/H₂O on the Surface of the Moon Seen by M3 on Chandrayaan-1. *Science* 326, 568-572.

Pommerol, A., Thomas, N., Affolter, M., Portyankina, G., Jost, B., Seiferlin, K., Aye, K.M., **2011**. Photometry and bulk physical properties of Solar System surfaces icy analogs: The Planetary Ice Laboratory at University of Bern. *Planetary and Space Science* 59, 1601-1612.

Pommerol, A., Jost, B., Poch, O., El-Maarry, M. R., Vuitel, B., and Thomas, N., **2015a**. The SCITEAS experiment: optical characterizations of sublimating icy planetary analogues. *Planetary and Space Science* 109-110, 106-122.

Pommerol, A., Thomas, N., El-Maarry, M.R., Pajola, M., Groussin, O., Auger, A.-T., Oklay, N., Fornasier, S., Feller, C., Davidsson, B., Gracia, A., Jost, B., Marschall, R., Poch, O., Barucci, M.A., Bertaux, J.-L., La Forgia, F., Keller, H.U., co-authors, **2015b**. OSIRIS observations of meter-size exposures of H₂O ice at the surface of 67P/Churyumov-Gerasimenko and interpretation using laboratory experiments. *Astronomy and Astrophysics*, in press.

Quirico, E., Montagnac, G., Lees, V., McMillan, P.F., Szopa, C., Cernogora, G., Rouzaud, J.N., Simon, P., Bernard, J.M., Coll, P., **2008**. New experimental constraints on the composition and structure of tholins. *Icarus* 198, 218-231.

Ratke, L., Kochan, H., **1989**. Fracture mechanical aspects of dust emission processes from a model comet surface, *Physics and Mechanics of Cometary Materials*, pp. 121-128.

Rosenthal, W., Saleta, J., Dozier, J., **2007**. Scanning electron microscopy of impurity structures in snow. *Cold Regions Science and Technology* 47, 80-89.

Sagan, C., Khare, B.N., **1979**. Tholins: organic chemistry of interstellar grains and gas. *Nature* 277, 102-107.

Saunders, S.R., Fanale, F.P., Parker, T.J., Stephens, J.B., Sutton, S., **1986**. Properties of filamentary sublimation residues from dispersions of clay in ice. *Icarus* 66, 94-104.

Sciamma-O'Brien, E., Carrasco, N., Szopa, C., Buch, A., Cernogora, G., **2010**. Titan's atmosphere: An optimal gas mixture for aerosol production? *Icarus* 209, 704-714.

Sciamma-O'Brien, E., Dahoo, P.R., Hadamcik, E., Carrasco, N., Quirico, E., Szopa, C., Cernogora, G., **2012**. Optical constants from 370 nm to 900 nm of Titan tholins produced in a low pressure RF plasma discharge. *Icarus* 218, 356-363.

Sears, D.W.G., Kochan, H.W., Huebner, W.F., **1999**. Laboratory simulation of the physical processes occurring on and near the surfaces of comet nuclei. *Meteoritics & Planetary Science* 34, 497-525.

Seiferlin, K., Spohn, T., Benkhoff, J., **1995**. Cometary ice texture and the thermal evolution of comets. *Advances in Space Research* 15, 35-38.

Sekanina, Z., **1991**. Cometary activity, discrete outgassing areas, and dust-jet formation, In: Newburn, R.L., Rahe, J.H. (Eds.), *Comets in the Post-Halley Era*. Springer.

Singer, R.B., McCord, T.B., Clark, R.N., Adams, J.B., Huguenin, R.L., **1979**. Mars surface composition from reflectance spectroscopy: A summary. *Journal of Geophysical Research: Solid Earth* 84, 8415-8426.

Storrs, A.D., Fanale, F.P., Saunders, R.S., Stephens, J.B., **1988**. The formation of Filamentary Sublimate Residues (FSR) from mineral grains. *Icarus* 76, 493-512.

Sunshine, J.M., A'Hearn, M.F., Groussin, O., Li, J.-Y., Belton, M.J.S., Delamere, W.A., Kissel, J., Klaasen, K.P., McFadden, L.A., Meech, K.J., Melosh, H.J., Schultz, P.H., Thomas, P.C., Veverka, J., Yeomans, D.K., Busko, I.C., Desnoyer, M., Farnham, T.L., Feaga, L.M., Hampton, D.L., Lindler, D.J., Lisse, C.M., Wellnitz, D.D., **2006**. Exposed Water Ice Deposits on the Surface of Comet 9P/Tempel 1. *Science* 311, 1453-1455.

Szopa, C., Cernogora, G., Boufendi, L., Correia, J.J., Coll, P., **2006**. PAMPRE: A dusty plasma experiment for Titan's tholins production and study. *Planetary and Space Science* 54, 394-404.

Thiel, K., Koelzer, G., Kochan, H., Ratke, L., Gruen, E., Koehl, H., **1989**. Dynamics of crust formation and dust emission of comet nucleus analogues under isolation, *Physics and Mechanics of Cometary Materials*, pp. 221-225.

Thomas, N., Sierks, H., Barbieri, C., Lamy, P.L., Rodrigo, R., Rickman, H., Koschny, D., Keller, H.U., Agarwal, J., A'Hearn, M.F., Angrilli, F., Auger, A.-T., Barucci, M.A., Bertaux, J.-L., Bertini, I., Besse, S., Bodewits, D., Cremonese, G., Da Deppo, V., Davidsson, B., De Cecco, M., Debei, S., El-Maarry, M.R., Ferri, F., Fornasier, S., Fulle, M., Giacomini, L., Groussin, O., Gutierrez, P.J., Güttler, C., Hviid, S.F., Ip, W.-H., Jorda, L., Knollenberg, J., Kramm, J.-R., Kührt, E., Küppers, M., La Forgia, F., Lara, L.M., Lazzarin, M., Moreno, J.J.L., Magrin, S., Marchi, S., Marzari, F., Massironi, M., Michalik, H., Moissl, R., Mottola, S., Naletto, G., Oklay, N., Pajola, M., Pommerol, A., Preusker, F., Sabau, L., Scholten, F., Snodgrass, C., Tubiana, C., Vincent, J.-B., Wenzel, K.-P., **2015**. The morphological diversity of comet 67P/Churyumov-Gerasimenko. *Science* 347.

Thompson, W.R., Murray, B., Khare, B., Sagan, C., **1987**. Coloration and darkening of methane clathrate and other ices by charged particle irradiation: Applications to the outer solar system. *Journal of Geophysical Research: Space Physics (1978–2012)* 92, 14933-14947.

Weiler, M., Rauer, H., Helbert, J., **2004**. Optical observations of Comet 67P/Churyumov-Gerasimenko. *Astronomy and astrophysics* 414, 749-755.

Weissman, P.R., **1986**. Are cometary nuclei primordial rubble piles? *Nature* 320, 242-244.